Journal of Hazardous Materials 445 (2023) 130593

Contents lists available at ScienceDirect

Journal of Hazardous Materials

journal homepage: www.elsevier.com/locate/jhazmat

Research Paper

Enhanced visible light assisted peroxymonosulfate process by biochar in-situ enriched with γ-Fe_2O_3 for p-chlorophenol degradation: performance, mechanism and DFT calculation

Chengyu Zhang [a,b,c], Zhisheng Yu [a,b,c,*], Xiangyang Wang [a,b,c], Bobo Wang [a,b,c]

[a] College of Resources and Environment, University of Chinese Academy of Sciences, 19 A Yuquan Road, Beijing 100049, PR China
[b] Binzhou Institute of Technology, Weiqiao-UCAS Science and Technology Park, Binzhou City 256606, Shandong Province, PR China
[c] RCEES-IMCAS-UCAS Joint-Lab of Microbial Technology for Environmental Science, Beijing 100085, PR China

HIGHLIGHTS

- The photocatalyst was obtained by biochar in-situ enriched with iron.
- The BF_γ/PMS/Vis system exhibited excellent performance and applicability.
- The 4-CP decomposition pathway and reactive mechanism were proposed.
- The formed C-O (C-Fe) bond and reduced band gap value enhanced the photocatalytic performance by DFT calculations.

GRAPHICAL ABSTRACT

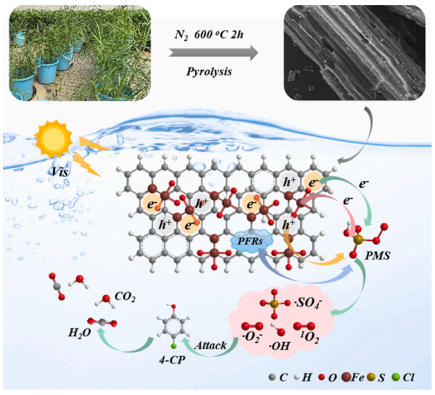

ARTICLE INFO

Editor: Yang Deng

Keywords:
Biochar
γ-Fe_2O_3
Peroxymonosulfate
Photocatalyst
P-chlorophenol, DFT calculations

ABSTRACT

In this study, a novel γ-Fe_2O_3/biochar (BF_γ) composite by a plant in-situ enrichment and one-step pyrolysis strategy was prepared, which was applied as a photocatalyst to activate peroxymonosulfate (PMS) for the degradation of p-chlorophenol (4-CP) under visible light irradiation (BF_γ/PMS/Vis) system. The characterization results exhibited that γ-Fe_2O_3 with localized carbon doping was evenly embedded in biochar during the pyrolysis. BF_γ exhibited better photoresponse properties than biochar (BC) and γ-Fe_2O_3. The removal efficiency of this system for 4-CP reached 96.41% under optimal conditions. This system showed high removal efficiency with a wide pH range (3.0–13.0) and under conditions of different organic pollutants. It also showed strong resistance to interference with co-existing inorganic ions and humic acid (HA). Electron paramagnetic resonance (EPR) and radical scavenging experiments revealed that the reactive oxygen species (ROS) in this system included $SO_4^{\cdot-}$, ·OH, $\cdot O_2^-$ and $^1O_2$. The density functional theoretical (DFT) calculations further revealed the promotion of localized carbon doping in γ-Fe_2O_3 on electron transfer and photoresponse, including C-O bond (d=1.29 Å), C-Fe

* Corresponding author at: College of Resources and Environment, University of Chinese Academy of Sciences, 19 A Yuquan Road, Beijing 100049, PR China.
E-mail address: yuzs@ucas.ac.cn (Z. Yu).

https://doi.org/10.1016/j.jhazmat.2022.130593
Received 28 July 2022; Received in revised form 31 October 2022; Accepted 10 December 2022
Available online 12 December 2022

bond (d=1.80 Å) and band gap value (E_{gap} < 0.72 eV). This study provides new insights into constructing environmentally-friendly catalysts and the possibility of the solid waste recycling for other wetland plants.

1. Introduction

Phenolic compounds are important chemical raw materials and chemical intermediates, which are widely used in the production and processing of dyestuffs, pesticides, adhesives and pharmaceutical intermediates (Dan et al., 2021). During the use and synthesis of phenolic compounds, phenol-containing wastewater is inevitably generated, which poses potential environmental risks to humans (Li et al., 2021c). And p-chlorophenol (4-CP) is one of the persistent organic pollutants that has attracted attention. There are adsorption (Gao et al., 2020; Hadi et al., 2020; Mao et al., 2021), membrane separation (Dharupaneedi et al., 2019; Zou et al., 2020), biological treatment(Li et al., 2020; Shi et al., 2022) and advanced oxidation processes (AOPs) (Jin and Dong, 2019; Yang et al., 2020) for 4-CP removal. Conventional procedures to remove 4-CP from aqueous solutions are ineffective because most of them are non-destructive, 4-CP is only transferred from aqueous solution to the solid phase(Eslami et al., 2018). In particular, AOPs is a process capable of generating free radicals (mainly hydroxyl radicals (·OH)) by various methods including photochemical, chemical, electrochemical, and sonochemical reactions (Belalcazar-Saldarriaga et al., 2018). AOPs is widely used because it can decompose 4-CP into low or non-toxic substances, or even directly mineralize them into carbon dioxide (CO_2) and water (H_2O) (Li et al., 2019; Zhang et al., 2022). AOPs based on peroxymonosulfate (PMS) have also attracted extensive attention due to their advantages such as faster reaction rate, stronger oxidation capacity, simpler operation and non-selectivity (Yang et al., 2022). PMS has been successfully applied to efficiently and rapidly degrade organic matter and disinfect bacteria (Rodríguez-Chueca et al., 2019). PMS is the main source of $SO_4^{\cdot-}$, which can be activated by thermal activation, alkaline activation, radiation activation, transition metal ions, metal oxides, and carbonaceous-based materials. Various activation methods have their shortcomings, so many researchers use two or more of them in combination to fully exploit their ability to remove organic pollutants (C and B, 2018). From the perspective of potential future applications, it is necessary to find nano-catalysts with a simple preparation process and low cost.

Metal-oxygen oxidants such as magnetite (Fe_3O_4), hematite (α-Fe_2O_3) and magnetite (γ-Fe_2O_3) with organics can form highly active intermediates, which are more active but unstable (Ma et al., 2019; Qin et al., 2021; Wang et al., 2021b). They quickly interact with organic matter to transform into stable products(Tian et al., 2019). Due to their excellent performances in catalyzing $SO_4^{\cdot-}$ generation (Rk et al., 2019) also have been explored by researchers. In particular, γ-Fe_2O_3 exhibits good photocatalytic performance for the degradation of organic pollutants and the production of hydrogen gas (Li et al., 2018; Ren et al., 2019). In the reaction process of catalyzing PMS, the catalyst can reduce Fe^{3+} to Fe^{2+} according to Eqs. (1)–(2) (Li et al., 2021a, Yi et al., 2020). However, its easy agglomeration causes a decrease in specific surface area, which results in a decrease in catalytic activity. Therefore, graphene oxide, bentonite and biochar can be used to reduce their agglomeration effect. Considering the requirements of sustainable development and low cost, biochar (BC) prepared from biomass is considered to be a versatile material for agricultural and environmental applications (Taskin et al., 2019), so it is a candidate material for the preparation of high-efficiency carbon-based catalysts as supports. It has been reported that BC can be used as a support for some metal oxides or metals to increase their specific surface area and thus promote their catalytic activity for PMS (Xu et al., 2021). BC has redox properties and can interact with ferrite through an electron transfer process (Tian et al., 2020) and organic pollutants can react directly with free radicals in BC (Dou et al., 2022). Furthermore, the presence of persistent free radicals (PFRs) (Luo et al., 2021), defect sites (Liang et al., 2021), nitrogen doping(You et al., 2021), and functional groups (Lee and Park, 2020) in the biochar sp^2 hybrid carbon matrix all contribute to the PMS activation of the free radical-generating redox process.

$$HSO_5^- + Fe^{3+} \rightarrow Fe^{2+} + SO_5^{\cdot-} + H^+ \quad (1)$$

$$HSO_5^- + Fe^{2+} \rightarrow Fe^{3+} + SO_4^{\cdot-} + OH^- \quad (2)$$

Herein, a novel γ-Fe_2O_3/biochar (BF_γ) prepared by a plant in-situ enrichment and one-step pyrolysis strategy, which was applied to activate PMS for the degradation of 4-CP under visible light irradiation (BF_γ/PMS/Vis) system. The effects of key parameters such as dosage of catalyst/PMS, coexisting ions and natural organic matter on 4-CP degradation in BF_γ/PMS/Vis system were investigated. The potential applications of this system including different organic pollutants (sulfamethoxazole (SMX), rhodamine B (RhB), tartrazine (TRZ) and carbamazepine (CBZ)), pH range, catalyst reuse and stability evaluation were explored. Finally, the mechanism of degradation/catalysis and possible for 4-CP degradation pathways were revealed by combining electron paramagnetic resonance (EPR), high-performance liquid chromatograph-mass spectrometer (HPLC-MS) and DFT theoretical calculation. This catalytic system provided an innovative and feasible treatment for the efficient degradation of the persistent organic pollutants in wastewater. Therefore, this study realized the resource utilization of solid waste containing metal ions in reeds and provided the possibility for the recycling of solid waste from other wetland plants.

2. Materials and methods

2.1. Materials

P-chlorophenol (4-CP, C_6H_5ClO, AR), sulfamethoxazole (SMX, $C_{10}H_{11}N_3O_3S$, AR), rhodamine B (RhB, $C_{28}H_{31}ClN_2O_3$, AR), carbamazepine (CBZ, $C_{15}H_{12}N_2O$, ≥99%) and tartrazine (TRZ, $C_{16}H_9N_4O_9S_2Na_3$, ≥99%) were obtained from Sinopharm Chemical Reagent Co. Ltd. Proxymonosulfate (PMS, $KHSO_5{\cdot}0.5KHSO_4{\cdot}0.5\ K_2SO_4$, 98%), sulfuric acid ($H_2SO_4$, 98.3%), ethanol (Et-OH, CH_3CH_2OH, AR), p-benzoquinone (p-BQ, AR), sodium azide (NaN_3, ≥99%), formic acid (FA, CH_2O_2, AR), potassium dichromate ($K_2Cr_2O_7$, AR) and tert-butanol (TBA, $C_4H_{10}O$, AR) were obtained from Sigma-Aldrich China. 5,5-Dimethyl-1-pyrroline N-oxide (AR) was obtained from Aladdin Chemistry Co., Ltd. Chromatographic grade methanol was obtained from Shanghai McLean Biochemical Technology Co., Ltd. Hoagland nutrient solution was purchased from Fuzhou Feijing Biological Technology Co., Ltd. Ultrapure water was used throughout the experiment. Each experiment was repeated three times to ensure the accuracy of the results.

2.2. Preparation of catalysts

Reed used widely in water environment remediation, so it was selected as the enrichment plant. The nutrient solution was changed regularly to ensure the concentration of iron ions (0.00 and 0.15 $g{\bullet}L^{-1}$) during the cultivation process. Additional hydroponics details are provided in Text S1 of Supplementary Material. The subsurface part of the reed was pyrolyzed in a vacuum tube furnace at 600 °C for 2 h under a nitrogen atmosphere (heating rate of 5 °C•min^{-1}). BC and BC enriched with γ-Fe_2O_3 (BF_γ) samples were obtained by grinding and passing through a 100-mesh sieve, respectively. The prepared samples were rinsed with ultrapure water, then placed in a vacuum drying oven at 60 °C for 48 h. Furthermore, the preparation method of γ-Fe_2O_3 was in Text S2.

2.3. Characterization of catalysts

The crystal phase of the samples was determined using an X-ray diffractometer (XRD, Smart Lab, Rigaku) via Cu-Kα radiation with 2θ range of 10–85°. The microscopic morphologies of the samples were recorded via scanning electron microscopy (SEM, SU8010, Hitachi) and energy dispersive spectroscopy (EDS). The microscopic morphology and lattice fringes of the samples were further measured by high-resolution transmission electron microscopy (HRTEM, 2100 F, JEM). The chemical species of the elements on the surface of the samples were determined via X-ray photoelectron spectroscopy (XPS, PHI-5700, ESCA). The specific surface area of the prepared samples was determined by the Brunel-Emmett-Taylor (BET) method. The electrochemical properties of the samples were measured by CHI660E electrochemical workstation. Reactive oxygen species (ROS) were identified using electron paramagnetic resonance spectrometer (EPR, A300–10/12, Bruker). The leaching amount of iron ions was measured via inductively coupled plasma optical emission spectrometry (ICP-MS, 7700, Agilent). The mineralization rate of organic pollutants was measured using a total organic carbon analyzer (TOC, TOC-1, Shimadzu).

2.4. Photocatalytic degradation experiments

The experimental reactions were carried out in a 150 mL beaker. Different catalysts (0.20 g•L^{-1}) were added to the aqueous solution of 4-CP (20 mg•L^{-1}), and stirred for 120 min under dark conditions to achieve saturated adsorption. Then PMS (300 mg•L^{-1}) was added to the reaction system, a 35 W xenon lamp was turned on at the same time. 1 mL of the solution was extracted from the reaction system and filtered through a 0.22 μm PTFE filter at times of 0, 5, 10, 30, 60, 90 and 120 min. The concentration of 4-CP was detected by high-performance liquid chromatography (HPLC). All experiments were carried out at 25 °C and the initial pH of the solution reaction was 6.1 ± 0.1 after the addition of PMS. BC, γ-Fe_2O_3 and BF_γ for the 4-CP degradation were investigated in different reaction systems to explore the catalyst performance.

3. Results and discussion

3.1. Characterization of the prepared catalysts

The crystal phase and phase purity of BC, γ-Fe_2O_3 and BF_γ were detected by XRD analysis. In Fig. 1, the diffraction peaks of BC including 20.6° (100), 26.6° (101), 36.5° (110), 39.5° (102), 50.1° (112), 60.0° (211) and 68.1° (203) were matched with SiO_2 (PDF#46–1045)(Chen et al., 2018). Characteristic diffraction peaks of γ-Fe_2O_3 (PDF#39–1346) at 30.2°, 35.6°, 43.3°, 53.7°, 57.3° and 62.9° were indexed to the (220), (311), (400), (422), (511) and (440) facets, respectively(Zhang et al., 2020). Moreover, the fairly sharp diffraction peaks indicated that the prepared γ-Fe_2O_3 sample was of high purity. The diffraction peak at 26.6° (005) in the BF_γ matched the diffraction peak of C (PDF#26–1077), which indicated a good degree of graphitization(Ding et al., 2021). More importantly, XRD results demonstrated the formation of hematite γ-Fe_2O_3 in BF_γ, and its sharp diffraction peaks indicated high crystallinity. Especially, the γ-Fe_2O_3 diffraction peaks in the BF_γ were shifted, which might be caused by the infiltration of surrounding carbon atoms into the γ-Fe_2O_3 crystal. The crystallite size of the samples was calculated using Scherer's formula(Shobha et al., 2019), expressed as Eq. (3):

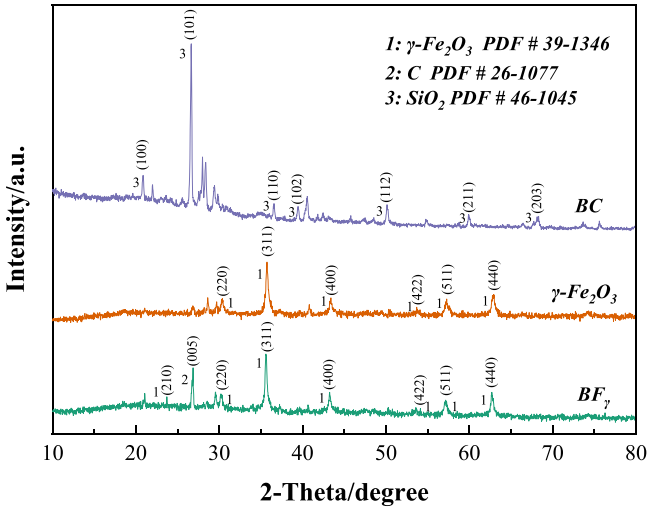

Fig. 1. XRD spectra of BC, γ-Fe_2O_3 and BF_γ.

$$D = \kappa \lambda / \beta \cos \theta \quad (3)$$

where D (nm) is the crystalline size, λ (0.1541 nm) is the X-ray wavelength, κ (0.94) is the shape factor, θ (°) is the half-angle in degrees, and β (rad) is the line broadening in half height. The crystal sizes of γ-Fe_2O_3 in BF_γ and γ-Fe_2O_3 samples were 31.5 nm and 26.0 nm by calculation, similar to the data of γ-Fe_2O_3 reported previously (Table S1) (Ates et al., 2020).

The morphologies of BC, γ-Fe_2O_3 and BF_γ samples were given in Fig. 2a–k. BC formed a porous structure during the pyrolysis process with a relatively smooth surface, showing a gauze-like appearance (Figs. 2a and 2b), γ-Fe_2O_3 presented an irregular granular shape (Figs. 2c and 2d), and BF_γ showed aggregated microspherical particles (Figs. 2e and 2f). Lattice fringes and symmetrical bright spots of BF_γ were observed from the TEM image (Fig. 2f), lattice diagram (Fig. 2g) and fast Fourier Transform pattern image (FFT) (Fig. 2h). The well-resolved (311) lattice plane corresponded to the spacing of 0.25 nm by measurement, which was consistent with the XRD results. The element mapping of BF_γ exhibited that γ-Fe_2O_3 was successfully and uniformly incorporated into biochar (Fig. 2i–k). EDX elemental mapping of BF_γ showed the mass of C, O and Fe were 85.07%, 10.85% and 4.08% (Fig. S1). There were many tiny γ-Fe_2O_3 nanoparticles aggregated on the surface of BF_γ, but it still endowed BF_γ with a large specific surface area. The BET measurement results showed that the specific surface areas of BC, γ-Fe_2O_3 and BF_γ were 21.27 m^2•g^{-1}, 17.32 m^2•g^{-1} and 38.24 m^2•g^{-1}, respectively (Table S2).

3.2. Electrochemical performance of the catalysts

PMS activation or pollutant-targeted degradation in visible-light photocatalytic degradation systems might be influenced by catalyst electron transfer properties (Yin et al., 2020b). Therefore, the photoelectrochemical properties of the prepared catalysts need to be evaluated by Tafel curves, linear sweep voltammetry (LSV) plots and electrochemical impedance spectroscopy (EIS) (Gandamalla et al., 2021). According to the Tafel curves of BC, γ-Fe_2O_3 and BF_γ samples (Fig. 3a), the corrosion current values were 7.32×10^{-7}, 2.37×10^{-5} and 4.21×10^{-5} A, respectively. BF_γ exhibited a higher corrosion current than the other two, indicating that it possessed excellent electron transfer properties and catalytic activity. Furthermore, it can be seen from the LSV plots that BF_γ exhibited higher current density than BC and γ-Fe_2O_3, indicating that BF_γ exhibited excellent electron transfer performance (Fig. 3b). The BF_γ under visible light irradiation had higher current densities and stronger photoresponsivity than dark conditions, indicating that visible light induced and promoted the generation of photogenerated electrons, which was consistent with literature reports (Ec et al., 2019). Compared to BC and γ-Fe_2O_3, the BF_γ under visible light exhibited smaller arc radius in the EIS curves (Fig. 3c), suggesting its smaller resistance. Therefore, the enhanced electron transfer properties of BF_γ might be due to the decrease in electrochemical impedance caused by the uniform distribution of γ-Fe_2O_3. In turn, these unhindered

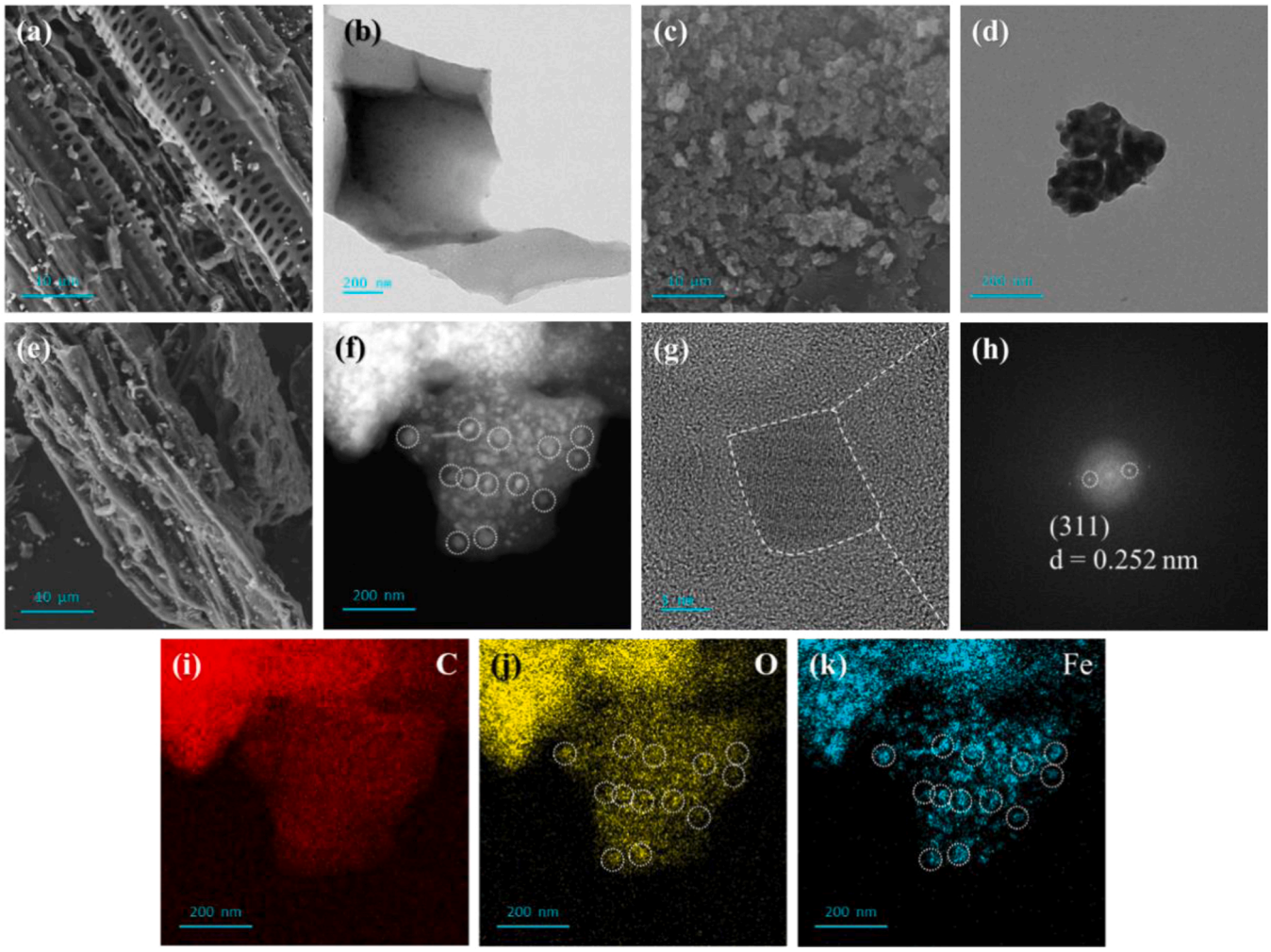

Fig. 2. SEM images of (a) BC, (c) γ-Fe_2O_3 and (e) $BF_γ$; HRTEM images of (b) BC, (d) γ-Fe_2O_3 and (f, g) $BF_γ$; Fast Fourier transformation (FFT) image of (h) $BF_γ$ and element mappings of (i, j, k) $BF_γ$.

electronic transitions made electron-dense regions active sites for reactions. Furthermore, unhindered electronic transitions in electron-dense regions could facilitate the PMS activation and induce the radical (or non-radical) decomposition reaction of organic pollutants (Guo et al., 2020).

3.3. Evaluation of the degradation performance of 4-CP

The degradation efficiency and mineralization efficiency of 4-CP in different systems were investigated to evaluate the catalytic performance of BC, γ-Fe_2O_3 and $BF_γ$. In Fig. 4a, the removal efficiencies of Vis-only, PMS-only and $BF_γ$-only systems were 14.08%, 13.93% and 13.44%, respectively, indicating that a single system could not effectively remove 4-CP. The removal efficiency of 4-CP by $BF_γ$/PMS system under the condition of the dark was only 42.37%. However, the degradation efficiency of 4-CP was further improved after adding PMS/Vis. The self-decomposition process of PMS under light irradiation might generate additional free radicals (Eq. (4)), which was beneficial for the decomposition of pollutants (He et al., 2022). In particular, the degradation efficiency of 4-CP reached 96.41% in 120 min in $BF_γ$/PMS/Vis system. As shown in Fig. 4b, the kinetics of the degradation curves of 4-CP could be represented via pseudo-first-order kinetic equation. In contrast, $BF_γ$/PMS/Vis system exhibited the highest rate constant (k) of 0.024 min^{-1} and the average half-life of 28.64 s. This might be due to the successful activation of the PMS (electron acceptor) by $BF_γ$ with the help of visible light, thereby generating plenty amount of reactive oxygen species (ROS, including ·OH, $SO_4^{\cdot-}$ and $^1O_2$) to achieve the degradation and mineralization of 4-CP (Xiong et al., 2021).

$$HSO_5^- + hv \rightarrow SO_4^{2-} + \cdot OH \quad (4)$$

According to the XRD data in Fig. 1, γ-Fe_2O_3 was generated in $BF_γ$ during the pyrolysis process. Therefore, to further evaluate the synergistic effect between γ-Fe_2O_3 and BC, different types of catalysts were prepared and their degradation efficiencies for 4-CP were investigated in different systems. As seen from Fig. 4c, the degradation efficiencies of BC singly in PMS, Vis and PMS/Vis systems were 24.97%, 21.03% and 32.41%, respectively. Furthermore, the degradation efficiencies of 4-CP via γ-Fe_2O_3/Vis, γ-Fe_2O_3/PMS and γ-Fe_2O_3/PMS/Vis systems were 21.36%, 31.24% and 42.11%, respectively. The degradation efficiencies of physically mixed γ-Fe_2O_3/BC/PMS, physically mixed γ-Fe_2O_3/BC/Vis system and γ-Fe_2O_3/BC /PMS/Vis system were 34.17%, 25.31% and 55.36%. Corresponding k values were 0.003 min^{-1},0.002 min^{-1} and 0.005 min^{-1} (Fig. 4d). This indicated that simple physical mixing could not effectively enhance the photocatalytic performance to degrade 4-CP. By calculation, the degradation efficiencies of 4-CP by $BF_γ$ in PMS/Vis system were 3.01 and 2.30 times that of BC and γ-Fe_2O_3, respectively. In addition, the mineralization efficiencies of the $BF_γ$/PMS/Vis, BC/PMS/Vis and γ-Fe_2O_3/PMS/Vis systems were 48.85%, 9.85% and 18.72%, respectively (Fig. 4e). The high mineralization efficiency of $BF_γ$/PMS/Vis system to 4-CP could effectively avoid secondary pollution of the environment by it and its intermediates. In general, the reason for this

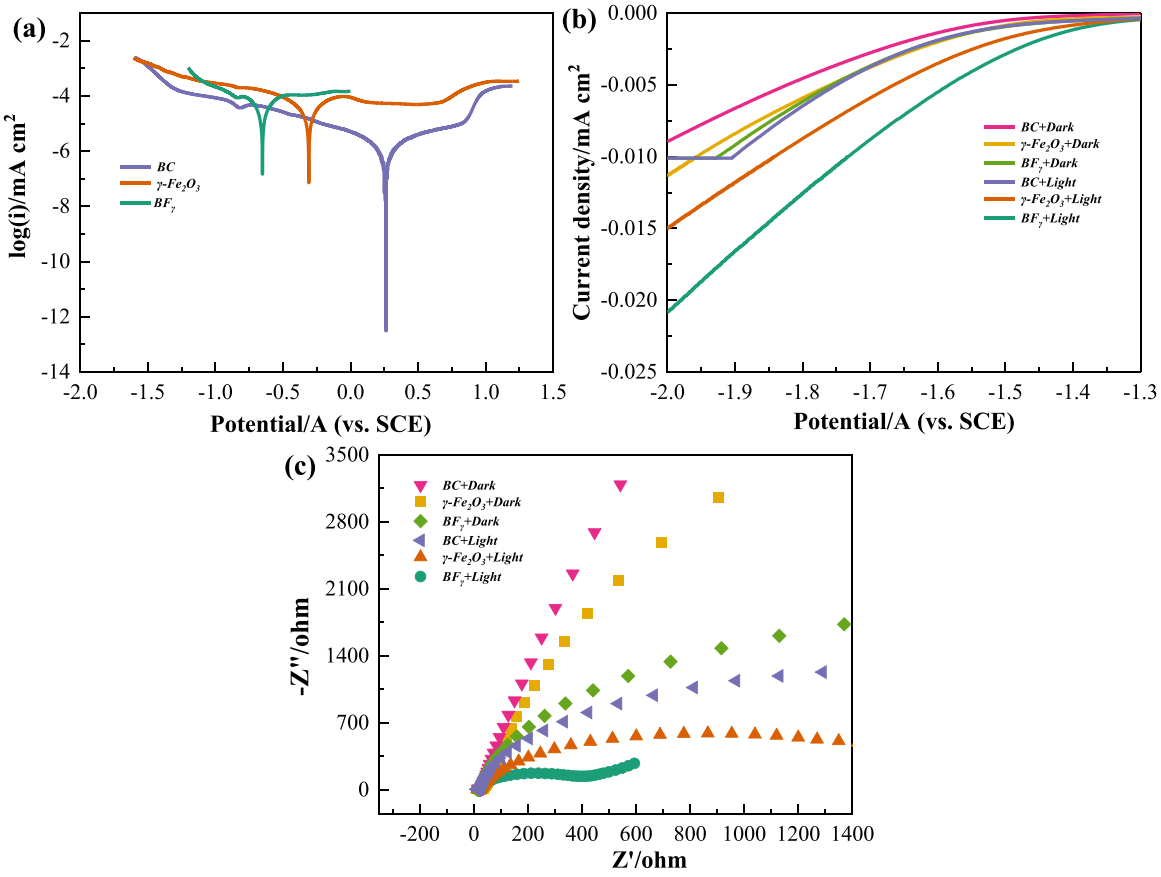

Fig. 3. (a) Tafel curves BC, γ-Fe_2O_3 and $BF_γ$, (b) linear sweep voltammetry plots and (c) electrochemical impedance spectroscopy spectra of BC, γ-Fe_2O_3 and $BF_γ$ under dark and light.

result should be related to the special spatial structure of the $BF_γ$ and the electrochemical performance. The $BF_γ$ with high electrochemical performance provided abundant reaction sites, and its special spatial structure enhanced the fast electron shuttle between carbon and γ-Fe_2O_3. These properties further induced the formation of ROS in PMS/Vis system, which destroyed organic pollutants.

3.4. Influences of key reaction parameters on the degradation of 4-CP

To optimize the experimental conditions, the influences of PMS dosage and $BF_γ$ dosage on the degradation efficiency of 4-CP were evaluated. As shown in Fig. 5a, the degradation efficiency of 4-CP increased by 15.14% (from 81.27% to 96.41%) when the dosage of PMS increased from 100 mg·L^{-1} to 300 mg·L^{-1}. Correspondingly, its k value increased by 35.79%. As the PMS dosage further increased, the increase in the degradation efficiency was not significant, and the corresponding k value increased by only 9.35%. As revealed in Fig. 5b, the degradation efficiency of 4-CP increased by 37.24% (from 59.17% to 96.41%) as the $BF_γ$ dosage increased from 0.05 g·L^{-1} to 0.20 g·L^{-1}, correspondingly, and the k value increased by 0.017 min^{-1}. However, no significant improvement in 4-CP degradation efficiency was observed with the increase of $BF_γ$ dosage from 0.20 g·L^{-1} to 0.40 g·L^{-1}. Overall, excess PMS and $BF_γ$ inhibited the efficient utilization of $SO_4^{\cdot-}$ and ·OH (Eqs. (5)–(7))(Liu et al., 2021). A similar phenomenon was also observed in previous literature(Kumar and Prasad, 2021). Considering the cost and the rising speed of the k value, the dosages of PMS and $BF_γ$ were selected as 300 mg·L^{-1} and 0.20 g·L^{-1}, respectively, as the optimal conditions for the reaction system.

$$SO_4^{\cdot-} + HSO_5^- \rightarrow SO_5^{\cdot-} + HSO_4^- \quad (5)$$

$$OH + HSO_5^- \rightarrow SO_5^{\cdot-} + H_2O \quad (6)$$

$$SO_4^{\cdot-} + SO_4^{\cdot-} \rightarrow S_2O_8^{2-} \quad (7)$$

Furthermore, the effect of different initial pH on the degradation efficiency of 4-CP was further evaluated. As shown in Fig. 5c, 4-CP was degraded by 87.83%, 91.65%, 96.41%, 97.66%, 88.71%, 82.58% and 78.59% under the initial pH of 3.0, 4.5, 6.1, 7.5, 9.0, 11.0 and 13.0, respectively. The degradation efficiency of 4-CP decreased with increasing pH (from 7.5 to 13.0), which might be due to the reaction between $SO_4^{\cdot-}$ and OH^- (Xie et al., 2019). Importantly, $BF_γ$/PMS/Vis system exhibited excellent 4-CP degradation efficiency at pH 6.1 and 7.5. Correspondingly, the k values were 0.025 min^{-1} and 0.028 min^{-1}, and the half-lives were 27.95 s and 24.88 s, respectively. Since the pH of most practical wastewaters was within 5.0–9.0 (Yin, R. et al., 2020a), $BF_γ$/PMS/Vis system could be applied to wastewater treatment.

The reusability of the catalyst was evaluated via cycle test of 4-CP degradation. It can be seen from Fig. 5d that $BF_γ$ after the first degradation reaction was washed with ultrapure water, and the degradation efficiency of 4-CP dropped sharply (only 62.19%) in the second cycle. As shown in Fig. 5d, the degradation efficiency of 4-CP washed with absolute ethanol (EtOH) was 85.46% after 5 degradation cycles. These results indicated that the organics adsorbed on the surface of $BF_γ$ could not be removed by simple water washing, but could be effectively removed by organic solvents (such as EtOH, methanol, etc.). Moreover, the active sites in $BF_γ$ maintained good stability during the degradation process. Importantly, the mineralization efficiency should also be concerned during the cyclic degradation of $BF_γ$. As shown in Fig. 5e, the mineralization efficiency decreased from 48.85% to 38.78% during the reuse of $BF_γ$. The reason for this result might be the leaching of iron ions in the acidic reaction solution, resulting in the loss of reaction sites.

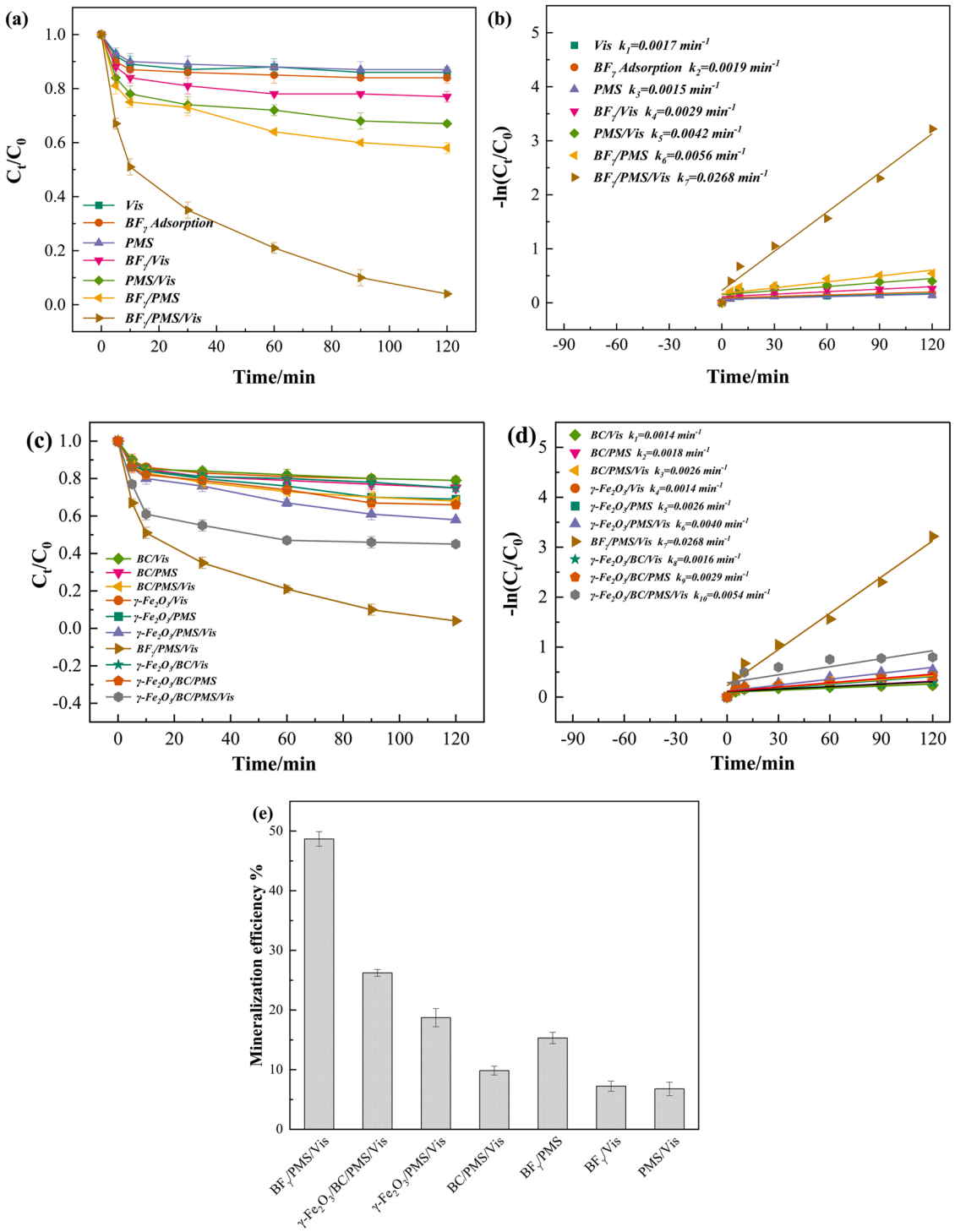

Fig. 4. (a, c) 4-CP degradation efficiency, (b, d) pseudo-first-order kinetics curves of 4-CP degradation efficiency and (e) mineralization efficiency in different reaction systems. (Reaction conditions: 4-CP = 20 mg·L^{-1}, catalyst dosage = 0.20 g·L^{-1}, PMS concentration = 300 mg·L^{-1} and initial pH = 6.1 ± 0.1).

3.5. Evaluation of applicability

3.5.1. Influence of inorganic ions and humic acid on the degradation of 4-CP

To explore the potential application value of BF_γ/PMS/Vis system in actual wastewater treatment, the influences of nitrate (NO_3^-), chloride (Cl^-), bicarbonate (HCO_3^-), ammonium salt (NH_4^+) and humic acid (HA) on the degradation efficiency of 4-CP were investigated. The addition of NO_3^- exhibited a significant negative effect on the degradation efficiency of 4-CP in BF_γ/PMS/Vis system (Fig. 6a). This might be due to the formation of $\cdot NO_3$, which could react with ·OH and $SO_4^{\cdot-}$ through NO_3^-, and its oxidizing capability was significantly reduced (Eqs. (8)–(9)) (Ouyang et al., 2019).

$$SO_4^{\cdot-} + NO_3^- \rightarrow \cdot NO_3 + SO_4^{2-} \quad (8)$$

$$OH + NO_3^- \rightarrow \cdot NO_3 + OH^- \quad (9)$$

Furthermore, Fig. 6b illustrated the influence of Cl^- introduction on the degradation efficiency of 4-CP. A significant inhibitory influence (5.01%) was observed in BF_γ/PMS/Vis system at low concentrations of

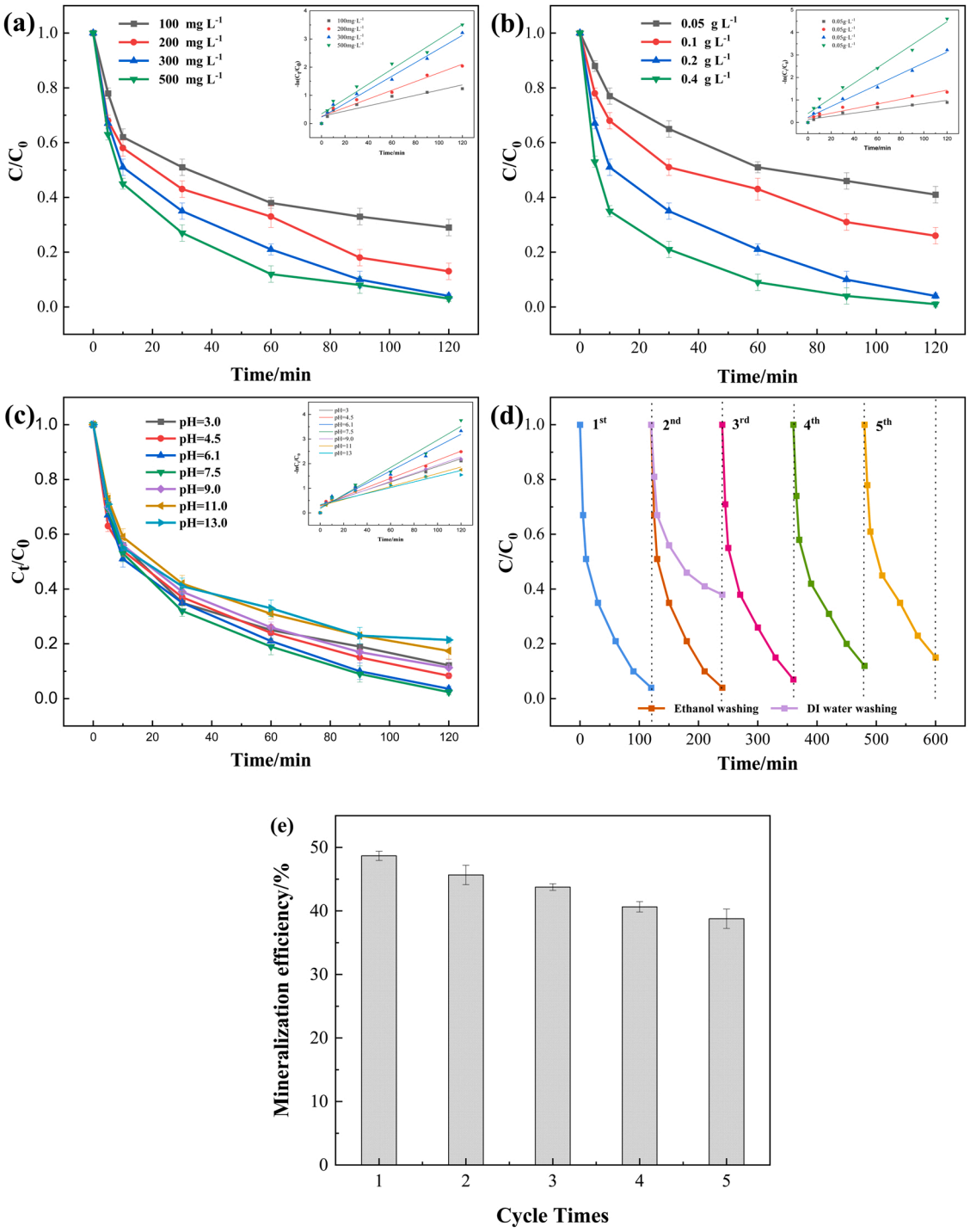

Fig. 5. (a) Influences of PMS dosage, (b) catalyst dosage, (c) different initial pH, (d) number of cycles and (e) mineralization efficiency after five cycles on BF_y/PMS/Vis system.

Cl^- (1 mM). This might be owed to the generation of chlorine radicals (Cl·) with low redox potential via the reaction between Cl^- and ROS (Eqs. (10)-(11)) (Li et al., 2021b). The degradation efficiency of 4-CP decreased with the further increase of Cl^- concentration, which was inhibited by 13.72% when the Cl^- concentration was 20 mM·L^{-1}. However, the degradation efficiency of 4-CP only decreased by 6.58% when the Cl^- concentration was increased from 20 to 40 mM·L^{-1}, which might be ascribed to the generated hypochlorous acid ($HClO^-$) via the reaction between Cl^- and PMS facilitating the decomposition of 4-CP (Eq. (12)) (Wang et al., 2021a).

$$SO_4^{\cdot-} + Cl^- \rightarrow SO_4^{\cdot-} + Cl \quad (10)$$

$$OH + Cl^- \rightarrow Cl\cdot + OH^- \quad (11)$$

$$HSO_5^- + Cl^- \rightarrow SO_4^{2-} + HClO^- \quad (12)$$

Especially, low concentrations (< 1 mM) of HCO_3^- effectively enhanced the degradation of 4-CP, while inhibition was evident at higher concentrations (Fig. 6c). Under low concentration conditions, HCO_4^- (1.8 V vs NHE) with high redox potential was produced by the nucleophilic reaction between HCO_3^- and PMS, which could directly

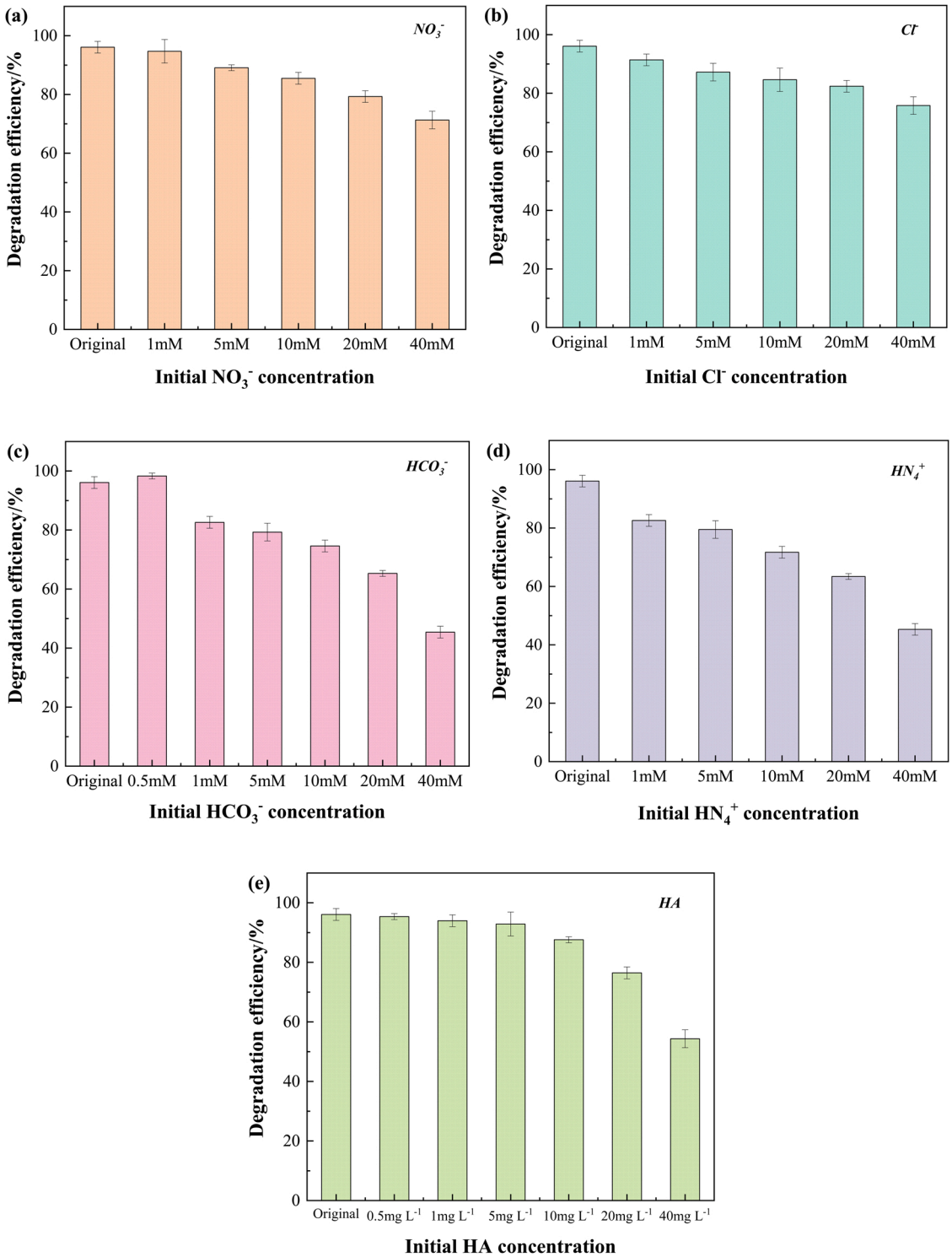

Fig. 6. (a) Influences of different inorganic ions and (b) humic acid on BF_Y/PMS/Vis system. (Reaction conditions: PMS concentration = 300 mg·L^{-1}, 4-CP = 20 mg·L^{-1}, catalyst dosage = 0.20 g·L^{-1}, and initial pH = 6.1 ± 0.1).

degrade 4-CP via single-electron reaction (Eqs. (13)-(14)) (Pan et al., 2021). However, carbonate free radicals ($CO_3^{\cdot-}$) with weak redox ability were generated in large quantities via the reaction between ROS and HCO_3^- at high concentrations (> 1 mM), resulting in a weakened oxidative activity of the system (Eqs. (15)-(16)) (Shao et al., 2020). The reaction solution gradually converted from acidic to basic (40 mM, pH = 8.55) with increasing HCO_3^- concentration (Fig. S3). This might facilitate the generation of ·OH through the reaction between $SO_4^{\cdot-}$ and OH^-,

resulting in the reduction of the degradation efficiency of 4-CP. Notably, $SO_4^{\cdot-}$ could maintain a stronger oxidation and longer lifetime at all pH conditions compared to ·OH (Dietrich and Burlingame, 2015). Furthermore, the introduction of high concentrations of NH_4^+ into BF_γ/PMS/Vis system also resulted in an increase in pH, which inhibited the degradation of 4-CP (Fig. 6d).

$$HCO_3^- + HSO_5^- \rightarrow SO_4^{2-} + HCO_4^- + H^+ \quad (13)$$

$$HCO_4^- + \text{4-CP} \rightarrow HCO_3^- + \text{products} \quad (14)$$

$$SO_4^{\cdot-} + HCO_3^- \rightarrow CO_3^{\cdot-} + SO_4^{2-} + H^+ \quad (15)$$

$$OH + HCO_3^- \rightarrow CO_3^{\cdot-} + H_2O \quad (16)$$

Besides, the influence of natural organic matter on the degradation of 4-CP could not be ignored in the reaction system. Humic acid (HA), a common natural organic matter, was selected for the experiments. As shown in Fig. 6e, the inhibition of HA on 4-CP degradation was not obvious at low concentrations (< 10 mg·L^{-1}), which might be related to the selectivity of the generated $SO_4^{\cdot-}$ in the BF_γ/PMS/Vis system for the degradation of organic matter (Xie et al., 2015). While the inhibition was significant at high concentrations (40 mg·L^{-1}) (Diao et al., 2019). This influence could be ascribed to two aspects: Plenty of HA was adhered to the surface of BF_γ sample under high concentration conditions, resulting in plenty of active sites being shielded; Furthermore, HA was generally regarded as a scavenger, resulting in a decrease in the degradation efficiency by competing with ROS in AOPs.

3.5.2. Degradation performance of the system to different organic pollutants

To explore the application of the system in organic wastewater remediation, the degradation efficiency and mineralization efficiency of different types of organic pollutants were investigated in BF_γ/PMS/Vis system (Fig. S2). The degradation efficiencies of the system for sulfamethoxazole (SMX), rhodamine B (RhB), tartrazine (TRZ) and carbamazepine (CBZ) were 95.36%, 97.47%, 94.32% and 90.25%, respectively (Fig. S2a). The above organic contaminants exhibited different physical and chemical properties because of their different molecular structures (Table S3). Hydroxyl (-OH) groups are prone to electrophilic reactions, which preferentially and selectively attack donor groups of organic molecules as reported (Xie et al., 2022). This led to the difference in the degradation efficiency of the organic contaminants via BF_γ/PMS/Vis system. Furthermore, the mineralization efficiencies of organic contaminants were evaluated by detecting the TOC removal efficiency and exhibited a good mineralization efficiency (> 45%) (Fig. S2b). In general, these results indicated the application prospect of BF_γ/PMS/Vis system for different refractory organic pollutants.

4. Mechanism of degradation and catalysis

4.1. Identification of the main reactive oxygen species

Biochar and its derivatives have been often used as catalysts in PMS systems to degrade organic pollutants in wastewater. The active sites and mechanisms of different biochar in PMS system were summarized in Table S4. The main reason for degrade organic pollutants was the production of ·OH. To investigate the generation pathway of ROS and its

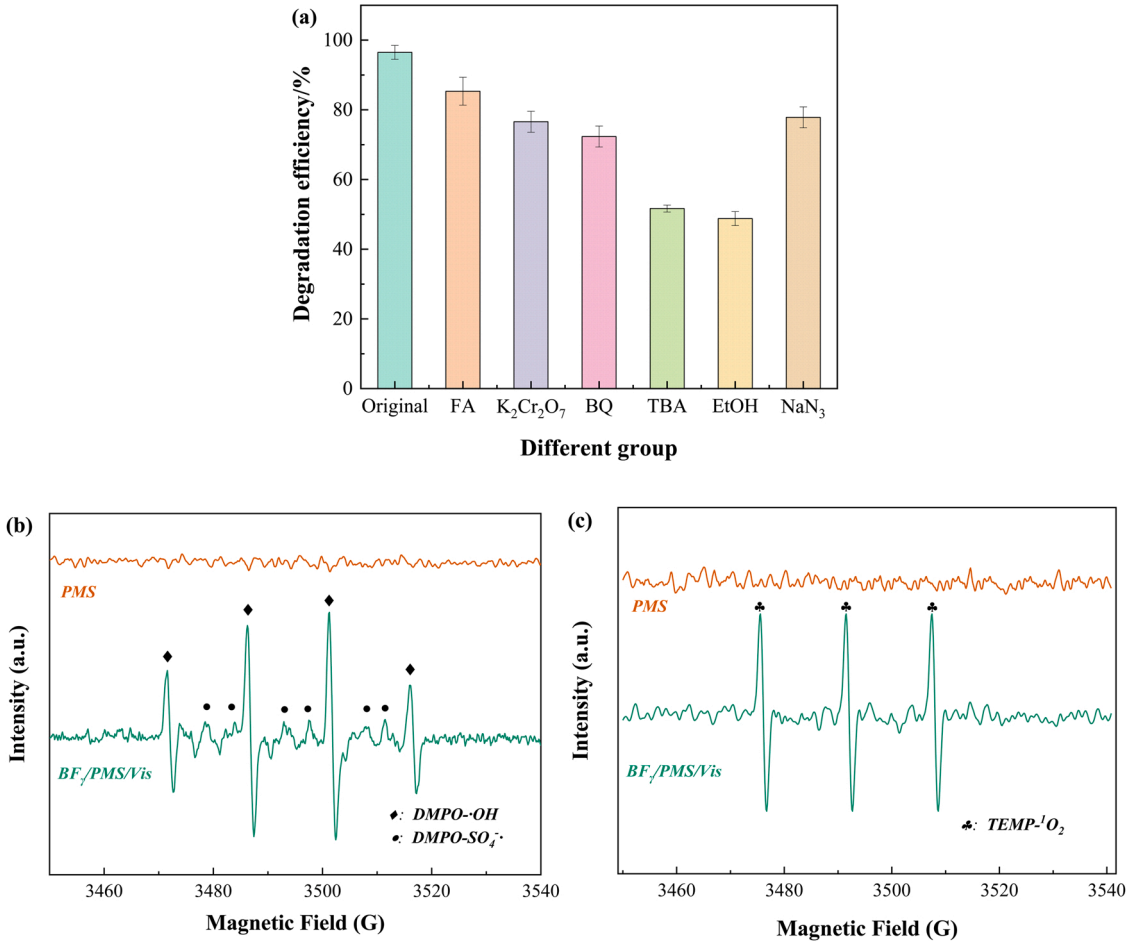

Fig. 7. (a) Influences of different radical quenchers on the degradation of 4-CP in BF_γ/PMS/Vis system. (b, c) EPR spectra in different systems.

influence on the degradation efficiency of 4-CP, tert-butanol (TBA), formic acid (FA), p-benzoquinone (BQ), potassium dichromate ($K_2Cr_2O_7$), ethanol (EtOH) and sodium azide (NaN_3) was used as a quencher for experiments. Specifically, EtOH is used as a quencher for ·OH and $SO_4^{\cdot-}$, FA, $K_2Cr_2O_7$, TBA, BQ and NaN_3 are typical quenchers for h^+, e^-, ·OH, $\cdot O_2^-$ and $^1O_2$, respectively (Zhu et al., 2021). The introduction of FA into BF_γ/PMS/Vis system led to a decay (from 96.41% to 85.34%) in 4-CP degradation (Fig. 7a), indicating that the photocatalytically generated holes (h^+) were involved in the reaction. The degradation efficiency of 4-CP decreased by 19.83% after quenching with $K_2Cr_2O_7$, which indicated that the electrons corresponding to the vacancies were involved in the oxidative degradation process. Importantly, the degradation efficiencies of 4-CP via EtOH and TBA were inhibited by 48.79% and 51.68%, respectively, suggesting that ·OH played an important role in the oxidation process. Besides, the degradation efficiencies of 4-CP were significantly decreased by adding BQ and NaN_3 alone (72.34% and 77.84%, respectively) to the system, indicating that $\cdot O_2^-$ and $^1O_2$ participated in the degradation of 4-CP. Overall, h^+, e^-, $SO_4^{\cdot-}$, ·OH, $\cdot O_2^-$ and $^1O_2$ generated in BF_γ/PMS/Vis system could all induce the decomposition of 4-CP.

To further verify that $SO_4^{\cdot-}$, ·OH and $^1O_2$ were generated in BF_γ/PMS/Vis system, EPR spectra were measured(Wen et al., 2022). From Figs. 7b and 7c, it can be seen that there was no obvious signal generation for DMPO and TEMP in the only-PMS system. Importantly, DMPO-·OH (relative intensity ratio, 1:2:2:1) and DMPO-$SO_4^{\cdot-}$ signals (relative intensity ratio, 1:1:1:1:1:1) were detected in BF_γ/PMS/Vis system. Compared with DMPO-$SO_4^{\cdot-}$, the DMPO-·OH exhibited a stronger signal, which might be ascribed to the formation of ·OH via the reaction between $SO_4^{\cdot-}$ and water molecules. (Eq. (17)). Notably, the characteristic peaks of TEMP-$^1O_2$ (relative intensity ratio, 1:1:1) were also detected in EPR testing, indicating the presence of $^1O_2$ (Fig. 7c).

$$SO_4^{\cdot-} + H_2O \rightarrow \cdot OH + SO_4^{2-} + H^+ \quad (17)$$

4.2. Intermediates and degradation pathways of 4-CP

To investigate the degradation mechanism, the intermediate

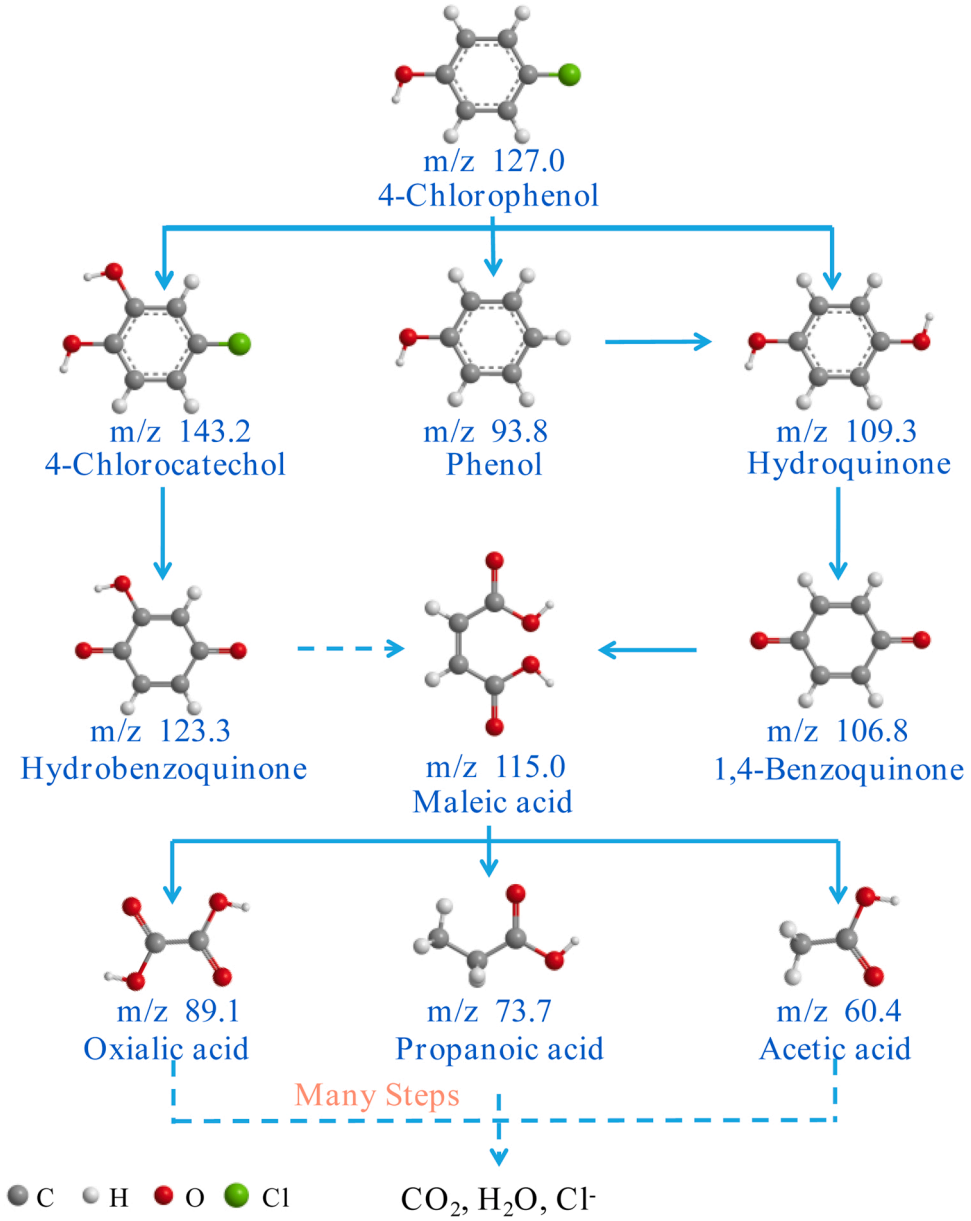

Fig. 8. The possible degradation pathways of 4-CP in BF_γ/PMS/Vis system.

products of 4-CP in BF_γ/PMS/Vis system were detected and analyzed via HPLC-MS (Liu et al., 2018). The possible degradation pathways were proposed based on the identified intermediates of 4-CP (Fig. 8). In addition to 4-chlorocatechol ($m/z = 143.2$), nine intermediates were detected including hydrobenzoquinone ($m/z = 123.3$), phenol ($m/z = 93.8$), hydroquinone ($m/z = 109.3$), 1,4-benzoquinone ($m/z = 106.8$), maleic acid ($m/z = 115.0$), oxalic acid ($m/z = 89.1$), propionic acid ($m/z = 73.7$) and acetic acid ($m/z = 60.4$) (Fig. S4). Furthermore, due to the strongly oxidizing properties of ROS, these intermediates were further mineralized to form CO_2, H_2O and Cl^- as the reaction proceeded. Notably, dechlorination, hydroxylation, and ring-opening might be important pathways during the degradation of 4-CP.

4.3. Catalytic mechanism of PMS

To explain the catalytic mechanism of BF_γ on PMS, the reacted materials were collected for characterization analysis. The XRD and XPS spectra of BF_γ were slightly changed before and after the reaction in PMS/Vis system (in Fig. 9a and 9b). The peak at 26.6° (005) in the BF_γ weakened after use, which might be due to the adsorption of a large number of intermediates of 4-CP on the material surface (Garba et al., 2019). In addition, the iron content in BF_γ after the reaction was detected by the microwave digestion method, which decreased by only 0.11% (Table S5). These results indicated that both the crystal structure and chemical composition of BF_γ remained stable in the reaction process. As shown in Fig. 9c-e, the characteristic peaks of C 1 S, O 1 S and Fe

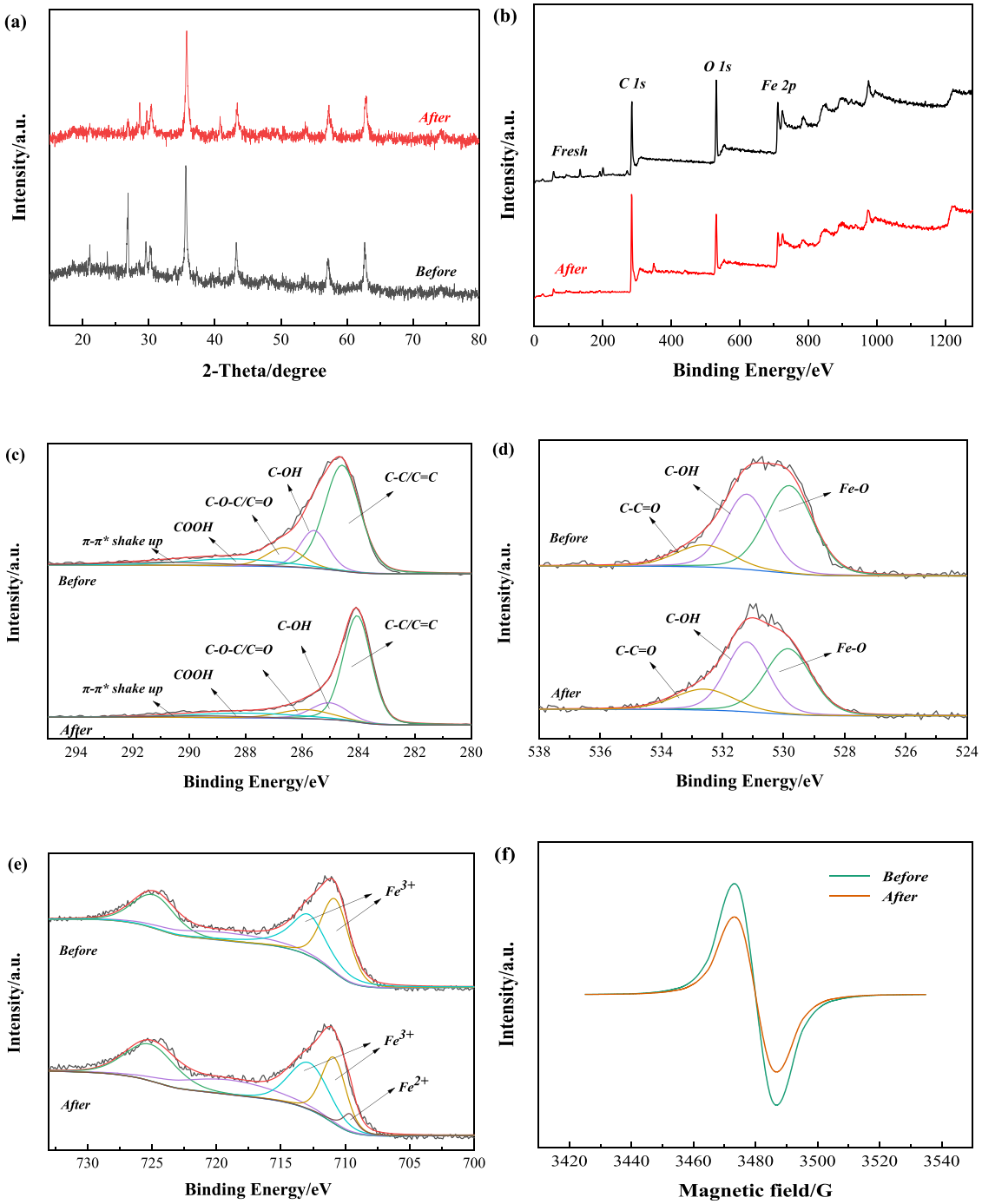

Fig. 9. (a) XRD spectra, XPS spectra of (b) the overall survey, (c) C 1 S, (d) O 1 S and (e) Fe 2 P, and (f) EPR spectra on BF_γ before and after the reaction.

2 P in XPS spectra were finely separated. The spectra of C1s were fitted to five peaks, including C═C/C-C (284.7 eV), C-OH (285.7 eV), C═O/C-O-C (286.6 eV), COOH (288.4 eV) and π-π * shake up (290.7 eV). As reported, the abundant oxygen functional groups and delocalized p electrons in carbon materials could transfer electrons into PMS to generate ROS (Eqs. (18)-(19)) (Hong et al., 2021; Wang et al., 2019). Table S6 showed the changes in surface functional groups before and after BF_γ obtained from XPS results. In particular, the relative contents of C-OH and π-π * shake-up were reduced by 2.37% and 4.34%, respectively, indicating that both participated in PMS activation. The O 1 S spectra were deconvoluted into three peaks, including Fe-O (530.3 eV), C-OH (531.6 eV) and C-C═O (533.0 eV). The relative contents of Fe-O decreased slightly, indicating the stability of the crystal phase of BF_γ. Moreover, the Fe $2p_{3/2}$ spectra of BF_γ were fitted to two peaks at 711.0 eV and 713.0 eV before the reaction, which was defined as Fe^{3+}. However, the peak of Fe^{2+} at 709.8 eV was observed after the reaction, which indicated that the electrons generated during the photocatalytic process reduced Fe^{3+} to Fe^{2+} (Eq. (20)) (Hu et al., 2020). Besides, there were slight blue shifts in the XPS spectra after the reaction, which was attributed to the deposition of intermediates on the surface of BF_γ. It was reported that the presence of Fe^{3+} in biomass promoted the generation of persistent free radicals (PFRs) in the pyrolysis process, and the massively generated PFRs also promoted the activation of PMS (Zeng et al., 2021). Therefore, the PFRs in BF_γ before and after the reaction were further detected via EPR (Fig. 9f). After the reaction, the content of PFRs in BF_γ decreased significantly, indicating that it participated in PMS activation.

$$BC_{surface}\text{-}OH + S_2O_8^{2-} \rightarrow SO_4^{-} + BC_{surface}\text{-}O\cdot + HSO_4^{-} \quad (18)$$

$$HSO_5^{-} + e^{-}(\pi\text{-}\pi^*) \rightarrow SO_4^{-}\cdot + OH^{-} \quad (19)$$

$$Fe^{3+} + e^{-} \rightarrow Fe^{2+} \quad (20)$$

According to all the above results, the possible activation mechanism of PMS was proposed in the reaction system. Specifically, the photogenerated electrons (e^-) completed the transition from the valence band (VB) to the conduction band (CB) when γ-Fe_2O_3 in BF_γ was placed under visible light irradiation. Correspondingly, plenty of h^+ was generated in VB (Eq. (21)) (Ma et al., 2018). As reported, the photogenerated electrons in pure ferric oxide would quickly recombine with h^+ and become inactive (Subha et al., 2022). In particular, a mass of photogenerated electrons was generated on the surface of BF_γ, which could then efficiently migrate via the carbon structure, thereby inhibiting the recombination of e^- and h^+ (Eq. (22)) (Hou et al., 2022). This indicated that BF_γ possessed a highly efficient electron transfer capability, which was consistent with the electrochemical measurements. Next, ROS were rapidly generated via the reaction between e^- and PMS, which further validated the results of the free radical quenching experiments (Eqs. (23)-(24)) (Ouyang et al., 2019). Moreover, the h^+ could not only react directly with 4-CP but also react with OH^- to generate ·OH (Eq. (25)) (Zhong et al., 2019).

Due to the superior capability of BF_γ to transfer electrons and visible light response, a high photocurrent was obtained by visible light irradiation. Notably, electron transfer enhanced the cycling of Fe^{3+}/Fe^{2+} (Eqs. (26)-(27)) (Zhang and Chu, 2022; Zhou et al., 2021), which was consistent with the XPS analysis. In particular, Fe^{3+} could directly react with PMS to form $SO_5^{-}\cdot$ with more selectivity (Eq. (27)). Furthermore, this radical could enhance the generation of ·OH Eq. (28) (Yu et al., 2021). According to previous researches and quenching experiments, $\cdot O_2^-$ could be induced via the reaction between PFRs and oxygen, and participated in PMS activation and organic pollutant decomposition (Eqs. (29)-(30)) (Liu et al., 2020a). Also, $^1O_2$ was generated in the system via the reaction between HSO_5^- and SO_5^{2-}, and participated in the degradation of 4-CP (Eq. (31)) (Liu et al., 2020b).

$$\gamma\text{-}Fe_2O_3 + \text{Visble Light} \rightarrow h^+/e^-(\gamma\text{-}Fe_2O_3) \quad (21)$$

$$e^-(\gamma\text{-}Fe_2O_3) \rightarrow e^-(BC) \quad (22)$$

$$HSO_5^- + e^-(BC) \rightarrow SO_4^-\cdot + OH^- \quad (23)$$

$$HSO_5^- + e^-(BC) \rightarrow SO_4^{2-} + \cdot OH \quad (24)$$

$$h^+(\gamma\text{-}Fe_2O_3) + OH^- \rightarrow \cdot OH \quad (25)$$

$$Fe^{2+} + HSO_5^- \rightarrow Fe^{3+} + OH^- + SO_4^- \quad (26)$$

$$Fe^{3+} + HSO_5^- \rightarrow Fe^{2+} + H^+ + SO_5^- \quad (27)$$

$$2SO_5^-\cdot + OH^- \rightarrow 2SO_4^{2-} + \cdot OH + O_2 \quad (28)$$

$$PFRs + O_2 \rightarrow product + \cdot O_2^- \quad (29)$$

$$HSO_5^- + \cdot O_2^- \rightarrow product + SO_4^- \quad (30)$$

$$HSO_5^- + SO_5^{2-} \rightarrow SO_4^{2-} + HSO_4^- + {}^1O_2 \quad (31)$$

4.4. DFT calculations

The above results exhibited that BF_γ could effectively enhance the photocatalytic performance via the plant enrichment method and one-step pyrolysis method. There might be two reasons for this: On the one hand, biochar inhibited the recombination of holes and electrons by rapidly transferring the photogenerated electrons of γ-Fe_2O_3, which was consistent with literature reports(Li et al., 2018); On the other hand, XRD spectra exhibited that γ-Fe_2O_3 crystal was infiltrated with carbon atoms, which might influence the band gap of γ-Fe_2O_3 and change the photocatalytic properties. Therefore, the role of carbon doping in γ-Fe_2O_3 was further investigated by density functional theory (DFT) calculation. As seen in Fig. 10, three configurations including pure γ-Fe_2O_3, interstitial C-doped γ-Fe_2O_3 and substitution C-doped γ-Fe_2O_3 were simulated. The stabilized surface structure and charge density of γ-Fe_2O_3 and C-doped γ-Fe_2O_3 on the (001) plane after structural optimization were exhibited in Fig. 10a. The bond length of the C-O bond ($d_{C\text{-}O}$=1.29 Å) in the gap doping was less than the sum of the atomic radius (d_{carbon}= 0.86 Å, d_{iron}= 0.66 Å) (Fig. 10b). Similarly, a C-Fe bond with a bond length of 1.80 Å was formed in alternative doping, which can be used as an electronic transfer channel (Fig. 10c). The inner charge density distribution of the pure γ-Fe_2O_3 was uniform. However, it could clearly see that the two doping modes causing that the local charge distribution was uneven. Overall, the doping of carbon in γ-Fe_2O_3 caused the bond formation and the re-allocation of the internal charge distribution, which was beneficial for the transport and transition of e^-. Furthermore, the band gap values and the projected density of states (PDOS) of pure γ-Fe_2O_3 and C-doped γ-Fe_2O_3 were calculated (Fig. S5). The band gap value of pure γ-Fe_2O_3 (0.72 eV) could be effectively reduced via interstitial (0.01 eV) or substitution doping (0.41 eV), which was beneficial for the transition of e^- from VB to CB. Also, the band gap value of carbon doping was closer to the conversion potential of radicals ($E(O_2/\cdot O_2^-) = -0.0046$ eV) than pure γ-Fe_2O_3 (Yang et al., 2019). Carbon doping could effectively reduce the band gap width of γ-Fe_2O_3, which was beneficial for the transition of e^- from VB to CB. The reduction of the band gap width was ascribed to the increase of the conduction band width due to the orbital hybridization induced by carbon doping via PDOS analysis. The above results proved that carbon doping could effectively adjust the photoresponse of γ-Fe_2O_3 crystal.

5. Conclusions

A novel BF_γ composite was fabricated using a plant in-situ enrichment and pyrolysis process, and used as a PMS catalyst under visible light irradiation. This preparation method achieved a uniform distribution of γ-Fe_2O_3 in biochar. BF_γ exhibited stronger visible light response and electron transfer ability than BC and pure γ-Fe_2O_3, which

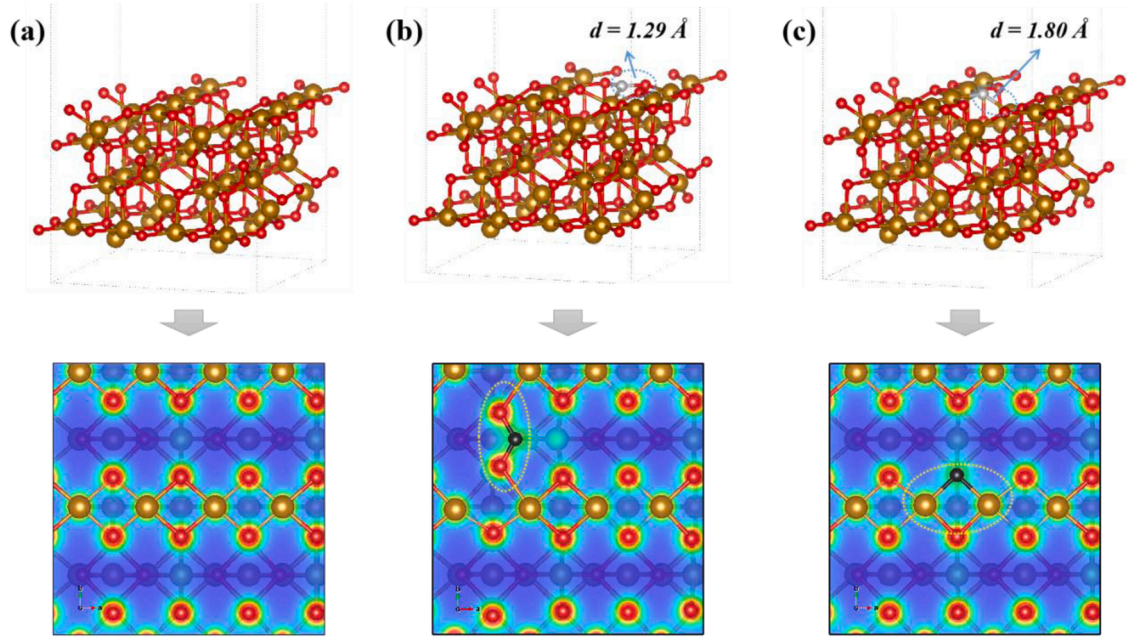

Fig. 10. Stable surface structure and charge densities of (a) pure γ-Fe_2O_3, (b) interstitial C-doped γ-Fe_2O_3 and (c) substitution C-doped γ-Fe_2O_3.

was manifested in stronger corrosion current (4.212×10^{-5} A), higher current density and lower resistance. BF_γ exhibited the excellent ability of PMS activation and generated amounts of intermediate reactive species during the reaction, including $SO_4^{\cdot-}$,$\cdot OH$,$\cdot O_2^-$, $^1O_2$, electron and hole. The removal efficiency of 4-CP could reach 96.41% at the conditions of PMS = 300 mg·L^{-1}, BF_γ = 0.20 g·L^{-1} and t = 120 min. Potential application capabilities of this system were also explored including a wide initial pH range (3.0–13.0), resistance to ion (NO_3^-, Cl^-, HCO_3^-, NH_4^+ and HA) interference and ability to remove different organic pollutants including SMX, RhB, TRZ and CBZ, accordingly, 95.36%, 97.47%, 94.32% and 90.25% of removal efficiencies. Possible degradation pathways of 4-CP were proposed including dechlorination, hydroxylation, and ring-opening. Finally, it was further revealed by DFT calculations that localized carbon doping in γ-Fe_2O_3 facilitated the delocalization of photogenerated electrons, thereby promoting the activation of PMS. In summary, this study provides a novel and environmentally friendly strategy to prepare iron/biochar composite with excellent catalytic ability.

Environmental implications

In this study, we ingeniously developed a novel photocatalyst of γ-Fe_2O_3-enriched biochar using a plant (reed) enrichment method and a simple one-step pyrolysis method. The evolution of reactive oxygen species and photogenerated electron transport pathways was investigated via experiments and DFT calculations. More importantly, the roles of localized carbon doping on electron transport and photoresponse in γ-Fe_2O_3 crystals were further evaluated. This provides a new feasible strategy for constructing environmentally friendly photocatalysts.

CRediT authorship contribution statement

Chengyu Zhang: Conceptualization, Methodology, Visualization, Writing – original draft, Writing – review & editing. **Xiangyang Wang:** Investigation, Writing – review & editing. **Bobo Wang:** Investigation, Writing – review & editing. **Zhisheng Yu:** Supervision, Resources, Writing – review & editing, Funding acquisition. All authors read and approved the final manuscript.

Declaration of Competing Interest

The authors declare that they have no known competing financial interests or personal relationships that could have appeared to influence the work reported in this paper.

Data Availability

Data will be made available on request.

Acknowledgments

This work was funded by Binzhou Institute of Technology (GYY–DTFZ–2022–003), and the Fundamental Research Funds for the Central Universities (E2E40503X2).

Appendix A. Supporting information

Supplementary data associated with this article can be found in the online version at doi:10.1016/j.jhazmat.2022.130593.

References

Ates, M., Cimen, I.C., Unal, I., Kutlu, B., Ertit Tastan, B., Danabas, D., Aksu, O., Arslan, Z., 2020. Assessment of impact of α-Fe_2O_3 and γ-Fe_2O_3 nanoparticles on phytoplankton species Selenastrum capricornutum and Nannochloropsis oculata. Environ. Toxicol. 35 (3), 385–394.

Belalcazar-Saldarriaga, A., Prato-Garcia, D., Vasquez-Medrano, R., 2018. Photo-Fenton processes in raceway reactors: technical, economic, and environmental implications during treatment of colored wastewaters. J. Clean. Prod. 182 (MAY 1), 818–829.

C, J.W.A.B., B, S.W.A., 2018. Activation of persulfate (PS) and peroxymonosulfate (PMS) and application for the degradation of emerging contaminants - ScienceDirect. Chem. Eng. J. 334, 1502–1517.

Chen, L., Yang, S., Zuo, X., Huang, Y., Cai, T., Ding, D., 2018. Biochar modification significantly promotes the activity of Co_3O_4 towards heterogeneous activation of peroxymonosulfate. Chem. Eng. J. 354, 856–865.

Dan, X., Luo, Z., Dai, M., Zhang, M., Yue, X., Xie, S., 2021. Oxidative degradation of p-chlorophenol by ferrate (VI): Kinetics, intermediates and pathways. J. Environ. Chem. Eng. 9 (4), 105810–105819.

Dharupaneedi, S.P., Nataraj, S.K., Nadagouda, M., Reddy, K.R., Shukla, S.S., Aminabhavi, T.M., 2019. Membrane-based separation of potential emerging pollutants. Sep. Purif. Technol. 210, 850–866.

Diao, Z.H., Dong, F.X., Yan, L., Chen, Z.L., Chu, W., 2019. Synergistic oxidation of Bisphenol A in a heterogeneous ultrasound-enhanced sludge biochar catalyst/

persulfate process: reactivity and mechanism. J. Hazard. Mater. 384, 121385–121394.
Dietrich, A.M., Burlingame, G.A., 2015. Critical review and rethinking of USEPA secondary standards for maintaining organoleptic quality of drinking water. Environ. Sci. Technol. 49 (2), 708–720.
Ding, Y., Li, Y., Dai, Y., Han, X., Xing, B., Zhu, L., Qiu, K., Wang, S., 2021. A novel approach for preparing in-situ nitrogen doped carbon via pyrolysis of bean pulp for supercapacitors. Energy 216, 119227–119239.
Dou, J., Cheng, J., Lu, Z., Tian, Z., Xu, J., He, Y., 2022. Biochar co-doped with nitrogen and boron switching the free radical based peroxydisulfate activation into the electron-transfer dominated nonradical process. Appl. Catal. B: Environ. 301, 120832–120844.
Ec, A., Gh, A., Xc, B., Feng, Z.A., Yd, A., Gy, A., Bl, A., Yw, C., 2019. In-situ hydrothermal fabrication of $Sr_2FeTaO_6/NaTaO_3$ heterojunction photocatalyst aimed at the effective promotion of electron-hole separation and visible-light absorption. Appl. Catal. B: Environ. 241, 52–65.
Eslami, A., Hashemi, M., Ghanbari, F., 2018. Degradation of 4-chlorophenol using catalyzed peroxymonosulfate with nano-MnO_2 /UV irradiation: toxicity assessment and evaluation for industrial wastewater treatment. J. Clean. Prod. 195 (SEP.10), 1389–1397.
Gandamalla, A., Manchala, S., Anand, P., Fu, Y.-P., Shanker, V., 2021. Development of versatile $CdMoO_4/g\text{-}C_3N_4$ nanocomposite for enhanced photoelectrochemical oxygen evolution reaction and photocatalytic dye degradation applications. Materials Today. Chemistry 19, 100392–100416.
Gao, Y., He, D., Wu, L., Wang, Z., Wang, M.X., 2020. Porous and ultrafine nitrogen-doped carbon nanofibers from bacterial cellulose with superior adsorption capacity for adsorption removal of low-concentration 4-chlorophenol. Chem. Eng. J. 8, 127411–127428.
Garba, Z.N., Zhou, W., Lawan, I., Xiao, W., Zhang, M., Wang, L., Chen, L., Yuan, Z., 2019. An overview of chlorophenols as contaminants and their removal from wastewater by adsorption: a review. J. Environ. Manag. 241, 59–75.
Guo, R., Wang, Y., Li, J., Cheng, X., Dionysiou, D.D., 2020. Sulfamethoxazole degradation by visible light assisted peroxymonosulfate process based on nanohybrid manganese dioxide incorporating ferric oxide. Appl. Catal. B: Environ. 278, 119297–119310.
Hadi, S., Taheri, E., Amin, M.M., Fatehizadeh, A., Aminabhavi, T.M., 2020. Adsorption of 4-chlorophenol by magnetized activated carbon from pomegranate husk using dual stage chemical activation. Chemosphere 270, 128623-123635.
He, Y., Qian, J., Wang, P., Wu, J., Lu, B., Tang, S., Gao, P., 2022. Acceleration of levofloxacin degradation by combination of multiple free radicals via MoS_2 anchored in manganese ferrite doped perovskite activated PMS under visible light. Chem. Eng. J. 431, 133933–133949.
Hong, Q., Liu, C., Wang, Z., Li, R., Ikhlaq, A., 2021. Electron transfer enhancing Fe(II)/Fe(III) cycle by sulfur and biochar in magnetic FeS@biochar to active peroxymonosulfate for 2,4-dichlorophenoxyacetic acid degradation. Chem. Eng. J. 417 (2), 129238–129252.
Hou, N., Li, X., Jiang, X., Zhang, N., Wang, R., Li, D., 2022. The role of biochar in the photocatalytic treatment of a mixture of Cr (VI) and phenol pollutants: Biochar as a carrier for transferring and storing electrons. Sci. Total Environ. 844, 157145–157157.
Hu, L., Liao, Y., Xia, D., Peng, F., Tan, L., Hu, S., Zheng, C., Lu, X., He, C., Shu, D., 2020. Engineered photocatalytic fuel cell with oxygen vacancies-rich $rGO/BiO_{1-x}I$ as photoanode and biomass-derived N-doped carbon as cathode: Promotion of reactive oxygen species production via Fe^{2+}/Fe^{3+} redox. Chem. Eng. J. 385, 123824–123838.
Jin, H., Dong, J., 2019. Enhanced performance of $Ag_3PO_4/Fe_3O_4/GO$ bifunctional catalysts on p-chlorophenol degradation in advanced catalytic oxidation systems. Colloids Surf. A: Physicochem. Eng. Asp. 581, 123803–123811.
Kumar, A., Prasad, B., 2021. Mechanistic approach of $SO_4^{\bullet-}/{\bullet}OH$ radical toward target pollutants degradation simultaneously enhanced activity and stability of perovskite-like catalyst $SrCu_xNi_{1-x}O_3$. Sep. Purif. Technol. 279, 119677–119692.
Lee, J.E., Park, Y.K., 2020. Applications of modified biochar-based materials for the removal of environment pollutants: a mini review. Sustainability 12 (15), 6112–6127.
Li, K., Ma, S., Xu, S., Fu, H., Li, Z., Li, Y., Liu, S., Du, J., 2021b. The mechanism changes during bisphenol A degradation in three iron functionalized biochar/peroxymonosulfate systems: the crucial roles of iron contents and graphitized carbon layers. J. Hazard. Mater. 404, 124145–124157.
Li, J., Yang, L., Lai, B., Liu, C., He, Y., Yao, G., Li, N., 2021a. Recent progress on heterogeneous Fe-based materials induced persulfate activation for organics removal. Chem. Eng. J. 414, 128674–128705.
Li, C., Yu, S., Che, H., Zhang, X., Han, J., Mao, Y., Wang, Y., Liu, C., Dong, H., 2018. Fabrication of Z-scheme heterojunction by anchoring mesoporous $\gamma\text{-}Fe_2O_3$ nanospheres on $g\text{-}C_3N_4$ for degrading tetracycline hydrochloride in water. ACS Sustain. Chem. Eng. 6 (12), 16437–16447.
Li, Y., Jiang, L., Wang, R., Wu, P., Zhu, N., 2021c. Kinetics and mechanisms of phenolic compounds by Ferrate(VI) assisted with density functional theory. J. Hazard. Mater. 415 (15), 125563–125573.
Li, L., Lai, C., Huang, F., Cheng, M., Zeng, G., Huang, D., Li, B., Liu, S., Zhang, M.M., Qin, L., 2019. Degradation of naphthalene with magnetic bio-char activate hydrogen peroxide: Synergism of bio-char and Fe-Mn binary oxides. Water Res. 160 (SEP.1), 238–248.
Li, Y., Zhao, J., Li, Y., Jin, B., Zhang, K., Zhang, H., 2020. Long-term alkaline conditions inhibit the relative abundances of tetracycline resistance genes in saline 4-chlorophenol wastewater treatment. Bioresour. Technol. 301, 122792–122801.
Liang, G., Yang, Z., Wang, Z., Cai, X., Zhang, X., Xie, X., 2021. Relying on the non-radical pathways for selective degradation organic pollutants in Fe and Cu co-doped biochar/peroxymonosulfate system: the roles of Cu, Fe, defect sites and ketonic group. Sep. Purif. Technol. 279, 119697–119710.
Liu, B., Guo, W., Wang, H., Si, Q., Zhao, Q., Luo, H., Ren, N., 2020a. Activation of peroxymonosulfate by cobalt-impregnated biochar for atrazine degradation: the pivotal roles of persistent free radicals and ecotoxicity assessment. J. Hazard. Mater. 398, 122768–122780.
Liu, L., Li, Y., Li, W., Zhong, R., Lan, Y., Guo, J., 2020b. The efficient degradation of sulfisoxazole by singlet oxygen ($^1O_2$) derived from activated peroxymonosulfate (PMS) with Co_3O_4–SnO_2/RSBC. Environ. Res. 187, 109665–109675.
Liu, L., Mi, H., Zhang, M., Sun, F., Zhan, R., Zhao, H., He, S., Zhou, L., 2021. Efficient moxifloxacin degradation by $CoFe_2O_4$ magnetic nanoparticles activated peroxymonosulfate: kinetics, pathways and mechanisms. Chem. Eng. J. 407, 127201–127212.
Liu, R., Xu, Y., Chen, B., 2018. Self-assembled nano-FeO (OH)/reduced graphene oxide aerogel as a reusable catalyst for photo-Fenton degradation of phenolic organics. Environ. Sci. Technol. 52 (12), 7043–7053.
Luo, K., Pang, Y., Wang, D., Li, X., Wang, L., Lei, M., Huang, Q., Yang, Q., 2021. A critical review on the application of biochar in environmental pollution remediation: Role of persistent free radicals (PFRs) - ScienceDirect. J. Environ. Sci. 108, 201–216.
Ma, Q., Zhang, X., Guo, R., Zhang, H., Cheng, Q., Xie, M., Cheng, X., 2019. Persulfate activation by magnetic $\gamma\text{-}Fe_2O_3/Mn_3O_4$ nanocomposites for degradation of organic pollutants. Sep. Purif. Technol. 210, 335–342.
Ma, Y., Wang, B., Wang, Q., Xing, S., 2018. Facile synthesis of α-FeOOH/$\gamma\text{-}Fe_2O_3$ by a pH gradient method and the role of $\gamma\text{-}Fe_2O_3$ in H_2O_2 activation under visible light irradiation. Chem. Eng. J. 354, 75–84.
Mao, S., Shen, T., Han, T., Ding, F., Zhao, Q., Gao, M., 2021. Adsorption and co-adsorption of chlorophenols and Cr (VI) by functional organo-vermiculite: Experiment and theoretical calculation. Sep. Purif. Technol. 277, 119638–119651.
Ouyang, D., Chen, Y., Yan, J., Qian, L., Han, L., Chen, M., 2019. Activation mechanism of peroxymonosulfate by biochar for catalytic degradation of 1, 4-dioxane: important role of biochar defect structures. Chem. Eng. J. 370, 614–624.
Pan, H., Gao, Y., Li, N., Zhou, Y., Lin, Q., Jiang, J., 2021. Recent advances in bicarbonate-activated hydrogen peroxide system for water treatment. Chem. Eng. J. 408, 127332–127345.
Qin, Q., Liu, T., Zhang, J., Wei, R., You, S., Xu, Y., 2021. Facile synthesis of oxygen vacancies enriched $\alpha\text{-}Fe_2O_3$ for peroxymonosulfate activation: a non-radical process for sulfamethoxazole degradation. J. Hazard. Mater. 419, 126447–126457.
Ren, L., Zhou, W., Sun, B., Li, H., Qiao, P., Xu, Y., Wu, J., Lin, K., Fu, H., 2019. Defects-engineering of magnetic $\gamma\text{-}Fe_2O_3$ ultrathin nanosheets/mesoporous black TiO_2 hollow sphere heterojunctions for efficient charge separation and the solar-driven photocatalytic mechanism of tetracycline degradation. Appl. Catal. B: Environ. 240, 319–328.
Rk, A., Bkb, C., Kg, D., Edf, C., Aa, E., 2019. Preparation, characterization and catalytic potential of $\gamma\text{-}Fe_2O_3$@AC mesoporous heterojunction for activation of peroxymonosulfate into degradation of cyfluthrin insecticide. Microporous Mesoporous Mater. 284, 111–121.
Rodríguez-Chueca, J., Giannakis, S., Marjanovic, M., Kohantorabi, M., Gholami, M.R., Grandjean, D., de Alencastro, L.F., Pulgarín, C., 2019. Solar-assisted bacterial disinfection and removal of contaminants of emerging concern by Fe^{2+}-activated HSO_5^- vs. $S_2O_8^{2-}$ in drinking water. Appl. Catal. B: Environ. 248, 62–72.
Shao, F., Wang, Y., Mao, Y., Shao, T., Shang, J., 2020. Degradation of tetracycline in water by biochar supported nanosized iron activated persulfate. Chemosphere 261, 127844–127853.
Shi, H., Jiang, X., Li, Y., Chen, D., Hou, C., Zhang, Z., Zhang, Q., Shen, J., 2022. Enhanced bio-photodegradation of p-chlorophenol by $CdS/g\text{-}C_3N_4$ 3D semiconductor-microbe interfaces. Sci. Total Environ. 807, 151006–151018.
Shobha, N., Nanda, N., Giresha, A.S., Manjappa, P., Sophiya, P., Dharmappa, K., Nagabhushana, B., 2019. Synthesis and characterization of Zinc oxide nanoparticles utilizing seed source of Ricinus communis and study of its antioxidant, antifungal and anticancer activity. Mater. Sci. Eng.: C. 97, 842–850.
Subha, N., Mahalakshmi, M., Monika, S., Kumar, P.S., Preethi, V., Vaishnavi, G., Rajabhuvaneswari, A., 2022. Heterostructured $\gamma\text{-}Fe_2O_3/FeTiO_3$ magnetic nanocomposite: An efficient visible-light-driven photocatalyst for the degradation of organic dye. Chemosphere 306, 135631–135639.
Taskin, E., de Castro Bueno, C., Allegretta, I., Terzano, R., Rosa, A.H., Loffredo, E., 2019. Multianalytical characterization of biochar and hydrochar produced from waste biomasses for environmental and agricultural applications. Chemosphere 233, 422–430.
Tian, S.Q., Wang, L., Liu, Y.L., Yang, T., Huang, Z.S., Wang, X.S., He, H.Y., Jiang, J., Ma, J., 2019. Enhanced permanganate oxidation of sulfamethoxazole and removal of dissolved organics with biochar: formation of highly oxidative manganese intermediate species and in situ activation of biochar. Environ. Sci. Technol. 53 (9), 5282–5291.
Tian, S.-Q., Wang, L., Liu, Y.-L., Ma, J., 2020. Degradation of organic pollutants by ferrate/biochar: Enhanced formation of strong intermediate oxidative iron species. Water Res. 183, 116054–116064.
Wang, R.-Z., Huang, D.-L., Liu, Y.-G., Zhang, C., Lai, C., Wang, X., Zeng, G.-M., Gong, X.-M., Duan, A., Zhang, Q., 2019. Recent advances in biochar-based catalysts: properties, applications and mechanisms for pollution remediation. Chem. Eng. J. 371, 380–403.
Wang, W., Liu, Y., Yue, Y., Wang, H., Cheng, G., Gao, C., Chen, C., Ai, Y., Chen, Z., Wang, X., 2021b. The confined interlayer growth of ultrathin two-dimensional Fe_3O_4 nanosheets with enriched oxygen vacancies for peroxymonosulfate activation. ACS. Catalysis 11 (17), 11256–11265.
Wang, Q., Xu, Z., Wang, S., Wang, Z., Jia, J., Li, H., Cao, Y., Chen, Y., Qin, Y., Cui, F., 2021a. Rapid synthesis of amorphous CoO nanosheets: Highly efficient catalyst for

parachlorophenol degradation by peroxymonosulfate activation. Sep. Purif. Technol. 263, 118369–118378.
Wen, Y., Huang, C.-H., Ashley, D.C., Meyerstein, D., Dionysiou, D.D., Sharma, V.K., Ma, X., 2022. Visible light-induced catalyst-free activation of peroxydisulfate: pollutant-dependent production of reactive species. Environ. Sci. Technol. 56 (4), 2626–2636.
Xie, M., Tang, J., Kong, L., Lu, W., Natarajan, V., Zhu, F., Zhan, J., 2019. Cobalt doped g-C_3N_4 activation of peroxymonosulfate for monochlorophenols degradation. Chem. Eng. J. 360, 1213–1222.
Xie, P., Ma, J., Liu, W., Zou, J., Yue, S., Li, X., Wiesner, M.R., Fang, J., 2015. Removal of 2-MIB and geosmin using UV/persulfate: contributions of hydroxyl and sulfate radicals. Water Res. 69, 223–233.
Xie, Z.-H., He, C.-S., Zhou, H.-Y., Li, L.-L., Liu, Y., Du, Y., Liu, W., Mu, Y., Lai, B., 2022. Effects of molecular structure on organic contaminants' degradation efficiency and dominant ros in the advanced oxidation process with multiple ROS. Environ. Sci. Technol. 56 (12), 8784–8795.
Xiong, Z., Jiang, Y., Wu, Z., Yao, G., Lai, B., 2021. Synthesis strategies and emerging mechanisms of metal-organic frameworks for sulfate radical-based advanced oxidation process: a review. Chem. Eng. J. 421, 127863–127895.
Xu, Y., Liu, S., Wang, M., Zhang, J., Ding, H., Song, Y., Zhu, Y., Pan, Q., Zhao, C., Deng, H., 2021. Thiourea-assisted one-step fabrication of a novel nitrogen and sulfur co-doped biochar from nanocellulose as metal-free catalyst for efficient activation of peroxymonosulfate. J. Hazard. Mater. 416, 125796-125717.
Yang, L., Liang, L., Wang, L., Zhu, J., Gao, S., Xia, X., 2019. Accelerated photocatalytic oxidation of carbamazepine by a novel 3D hierarchical protonated g-C_3N_4/BiOBr heterojunction: performance and mechanism. Appl. Surf. Sci. 473, 527–539.
Yang, L., Yang, H., Yin, S., Wang, X., Xu, M., Lu, G., Liu, Z., Sun, H., 2022. Fe single-atom catalyst for efficient and rapid fenton-like degradation of organics and disinfection against bacteria. Small 2104941–2104955.
Yang, Y., Li, X., Zhou, C., Xiong, W., Zeng, G., Huang, D., Zhang, C., Wang, W., Song, B., Tang, X., 2020. Recent advances in application of graphitic carbon nitride-based catalysts for degrading organic contaminants in water through advanced oxidation processes beyond photocatalysis: a critical review. Water Res. 184, 116200–116218.
Yi, Q., Liu, W., Tan, J., Yang, B., Xing, M., Zhang, J., 2020. Mo0 and Mo^{4+} bimetallic reactive sites accelerating Fe^{2+}/Fe^{3+} cycling for the activation of peroxymonosulfate with significantly improved remediation of aromatic pollutants. Chemosphere 244, 125539–125549.
Yin, R., Chen, Y., He, S., Li, W., Zeng, L., Guo, W., Zhu, M., 2020a. In situ photoreduction of structural Fe (III) in a metal–organic framework for peroxydisulfate activation and efficient removal of antibiotics in real wastewater. J. Hazard. Mater. 388, 121996–122116.
Yin, Z., Han, M., Hu, Z., Feng, L., Liu, Y., Du, Z., Zhang, L., 2020b. Peroxymonosulfate enhancing visible light photocatalytic degradation of bezafibrate by Pd/g-C_3N_4 catalysts: the role of sulfate radicals and hydroxyl radicals. Chem. Eng. J. 390, 124532–124543.
You, Y., Zhao, Z., Song, Y., Li, J., Cheng, X., 2021. Synthesis of magnetized nitrogen-doped biochar and its high efficiency for elimination of ciprofloxacin hydrochloride by activation of peroxymonosulfate. Sep. Purif. Technol. 258, 117977–117988.
Yu, X., Qin, W., Yuan, X., Sun, L., Pan, F., Xia, D., 2021. Synergistic mechanism and degradation kinetics for atenolol elimination via integrated UV/ozone/peroxymonosulfate process. J. Hazard. Mater. 407, 124393–124402.
Zeng, L., Chen, Q., Tan, Y., Lan, P., Zhou, D., Wu, M., Liang, N., Pan, B., Xing, B., 2021. Dual roles of biochar redox property in mediating 2, 4-dichlorophenol degradation in the presence of Fe^{3+} and persulfate. Chemosphere 279, 130456–130464.
Zhang, S., Liu, Y., Ma, R., Jia, D., Wen, T., Ai, Y., Zhao, G., Fang, F., Hu, B., Wang, X., 2022. Molybdenum (VI)-oxo clusters incorporation activates g-C_3N_4 with simultaneously regulating charge transfer and reaction centers for boosting photocatalytic performance. Adv. Funct. Mater. 32 (38), 2204175–2204187.
Zhang, Y., Chu, W., 2022. g–C_3N_4 induced acceleration of Fe^{3+}/Fe^{2+} cycles for enhancing metronidazole degradation in Fe^{3+}/peroxymonosulfate process under visible light. Chemosphere 293, 133611–133622.
Zhang, Y., Su, P., Weathersby, D., Zhang, Q., Zheng, J., Fan, R., Zhang, J., Dai, Q., 2020. Synthesis of γ-Fe_2O_3-ZnO-biochar nanocomposites for Rhodamine B removal. Appl. Surf. Sci. 501, 144217–144224.
Zhong, J., Zhao, Y., Ding, L., Ji, H., Ma, W., Chen, C., Zhao, J., 2019. Opposite photocatalytic oxidation behaviors of BiOCl and TiO_2: direct hole transfer vs. indirect OH oxidation. Appl. Catal. B: Environ. 241, 514–520.
Zhou, H., Zhang, H., He, Y., Huang, B., Zhou, C., Yao, G., Lai, B., 2021. Critical review of reductant-enhanced peroxide activation processes: Trade-off between accelerated Fe^{3+}/Fe^{2+} cycle and quenching reactions. Appl. Catal. b: Environ. 286, 119900–119920.
Zhu, G., Zhu, J., Liu, Q., Fu, X., Chen, Z., Li, K., Cao, F., Qin, Q., Jiao, M., 2021. HPO_4^{2-} enhanced catalytic activity of N, S, B, and O-codoped carbon nanosphere-armored Co_9S_8 nanoparticles for organic pollutants degradation via peroxymonosulfate activation: critical roles of superoxide radical, singlet oxygen and electron transfer. Phys. Chem. Chem. Phys. 23 (9), 5283–5297.
Zou, Q., Zhang, Z., Li, H., Pei, W., Ding, M., Xie, Z., Huo, Y., Li, H., 2020. Synergistic removal of organic pollutant and metal ions in photocatalysis-membrane distillation system. Appl. Catal. B: Environ. 264, 118463–118473.